Graphene Plasmonics for Surface-Enhanced Infrared Spectroscopy

Alexander Plyushch

PREFACE

Experimental and computational work for the actual thesis was conducted during May 2019 - June 2020 at the Department of Physcis at the University of Jyväskylä. Unfortunately, due to the global pandemic situation of the year 2020, the experimental work has not been finished. The latest obtained experimental results are demonstrated nevertheless.

I would like to express my deepest appreciation to my supervisors, Toppari Jussi and Johansson Andreas, for giving an opportunity to conduct this research and for invaluable support and guidance provided. It was my pleasure and luck to work under such a competent supervision.

I would like to extend my sincere thanks to doctoral students and personnel of the Nanoscience Center for helping along with practicalities and the equipment. Special thanks to Manninen Jyrki and Hiltunen Vesa-Matti, for their time and assistance with fabrication and measurement related matters, and Dutta Arpan, for the helping with numerical simulations.

I also wish to thank teachers and administration of the Department of Physics of the University of Jyväskylä for providing the outstanding quality of education and research, and building scientific community and atmosphere.

Lastly, I would like to thank my dear wife, Polina, for all the support and encouragement during the writing of this thesis.

ABSTRACT

The work, presented in this thesis, focuses on studying graphene as a signal enhancing material for spectroscopic applications. Among many outstanding characteristics of graphene, it also exhibits attractive plasmonic properties. Tunability of the resonance within THz to Mid-IR range and high field confinement factor makes it a great candidate for the surface enhanced infrared spectroscopy application. This thesis presents the results of computational and experimental investigation of graphene-based optical resonators. The numerical study was focused on the optimization of two-dimensional graphene geometries, looking to achieve the highest enhancement factor. The experimental part of the work included the fabrication process optimization and characterization of produced graphene structures.

Numerical simulations of plasmonic resonance of structured graphene at far infrared range was performed using Finite-Difference Time-Domain method. Simulated results demonstrated the possibility to achieve the enhancement factor of $\approx 10^5$ for near-field coupled structures spaced as close as 10 nm. Two-dimensional periodicity of studied geometries demonstrated switchable resonance modes, accessible via polarization of the incident light. Numerical studies also revealed a substantial degradation of the enhancement factor related to the quality of graphene.

The experimental work consisted of the optimization of graphene patterning process, fabrication of the active plasmonic device and its characterization using FTIR microscopy and scanning probe imaging. A novel approach for graphene patterning was utilized. Substituting the conventional lithography, focused ion beam was used to selectively remove graphene, producing high-resolution patterns. Surface profile imaging of milled structures demonstrated an excellent performance and accuracy for 30 keV neon beam. FTIR measurements did not produce the reliable results. Observed spectral variations are not certain to be caused by plasmonic excitations. The uncertainty of infrared absorption measurements may be linked to the overall design of the device and the fabrication method chosen. Further discussion is given in the thesis.

CONTENTS

1. INTRODUCTION

Since the ancient times, people have been trying to manipulate the light. The first documented usage of lenses or "crystals used to kindle fire" dates back to 450-385 BC. And only 400 years later, in the Roman Empire, lenses started to be used as a magnifying tool [1]. However, only during the past century and a half a solid theoretical foundation has emerged. The works of Maxwell, quantum theory and special relativity allowed an in depth understanding of the behavior of light and its interaction with matter. These breakthroughs pushed the development in the field of optics and gave birth to sub-fields such as photonics, quantum optics, optomechanics and others.

Plasmonics is a sub-field of photonics that explicitly focuses on hybrid light-matter modes - the interaction between electrons in matter and electromagnetic field. From the viewpoint of plasmonics, the electrons in matter can be approximated as a gas of charges, plasma, which can fluctuate when being subjected to an oscillating electromagnetic fields. The coupling between both systems causes electromagnetic waves to be confined in a sub-wavelength dimensions, with large near-field enhancement. What makes this field especially intriguing is the geometric dependency of plasmonic excitation. In the case of 2-dimensional metal-dielectric interfaces, a coupled portion of the incident electromagnetic radiation can propagate along the surface in a form of *surface plasmon polariton* (*SPP*). The other, non-propagating, type of plasmon resonance occurs in metallic structures with sub-wavelength dimensions and is known as *localised surface plasmon* (*LSP*). These excitation types are the two main pillars of plasmonic research which focuses on fabrication, characterization, modeling and applications of plasmonic nanostructures and interfaces.

The first piece of theory on the plasmonic effect can be found in the work of Sommerfeld [2] published in 1899. This publication presents a mathematical model describing propagation of electromagnetic waves along the surface of material. A strong impulse for the development in the field, however, was generated by Wood [3] attempting to investigate an anomaly in the absorption spectrum of the metallic grating. It took almost half a century and groundbreaking emergence of quantum theory, to interpret Wood's anomaly. The first notable works explaining Wood's observation were published by Fano [4], Hessel on Oliner [5], and Ritchie et al. [6]. These works firmly established a mathematical description of SPP phenomena. The concept was further developed by Kretschmann and Raether [7] along with Otto [8], who introduced a technique of coupling the light to surface plasmons using a prism. The description of localzed surface plasmons were first presented by Mie in 1908 [9].

The rapid development of nanofabrication techniques along with computational mod-

1

eling allowed utilization of the plasmonic effect in numerous applications, including, but not limited to, energy production [10], optics [11] and lasers [12], medical diagnostics [13], biosensing [14], spectroscopy [15]. Currently, the research on the fundamental properties of plasmonics is focused to get a deeper insight into the nature and properties of plasmons. Among the latest topics are quantum plasmonics [16], nonlinear plasmonics [17], the strong coupling between SPP and electronic states [18], [19], and ultra-fast plasmonics [20].

This work focuses on studying plasmonic excitation in graphene. Since the discovery of a reliable isolation method by Novoselov and Geim [21], graphene became a hot topic for many research groups all over the world due to its outstanding optical, [22], electronic [23], and mechanical [24] properties. Graphene, a carbon allotrope, is a single-layer crystal of carbon atoms arranged in a honeycomb pattern. It is a truly two-dimensional material with unique semiconducting properties arising from its electron bandstructure.

Many potential application and unusual properties of graphene has been reported since its discovery and plasmonics is among them. The first paper on plasmonic effect in graphene was published in 2011 by Ju et al. [25]. The paper demonstrated the possibility of excitation of localised surface plasmons in graphene by patterning it into an array of uniformly spaced ribbons. Several research groups around the globe began to explore that topic since then. The most prominent results are published by Bludov et al. [26], Garcia de Abajo [27], Avouris and Low [28], Koppens et al. [29], and Stauber [30]. Unlike noble metals, typically used as plasmonic materials, graphene demonstrated additional tunability of plasmonic resonance via electrostatic gating or chemical doping. It is a crucial advantage of graphene, enabling a post-fabrication adjustment of resonant frequency. Other notable properties of graphene-based plasmons is a stronger light-confinement factor compared to metals and active spectral range from several THz to far-infrared.

Here, in this work, plasmonic properties of graphene are studied from the perspective of spectroscopy enhancement and sensing. The applicability of graphene in this area has already been demonstrated by Rodrigo et al. [31], Hai et al. [32], Marini et al. [33] and several others [34]–[36]. Graphene has demonstrated sufficient signal enhancement for infrared absorption spectroscopy, Raman spectroscopy and refractive-index sensing. For Raman scattering, the enhancement pathway of graphene is not fully related to the plasmonic phenomena, but also to its chemical activity. FTIR and sensor signals, however, are enhanced via purely plasmonic excitations in the nanostructured graphene. The field of graphene-based plasmon-enhanced spectroscopy is still at the early stage of development. The major issue with graphene in any electronic application is an insufficient quality of fabricated layers and inability to deposit them directly onto a semiconductor surface, such

as commonly used silicon. Due to a multi-stage synthesis and transfer procedure, the electrical properties of fabricated graphene are compromised [37]. This leads to an weak signal produced by graphene plasmonic structures. The sensitivity and signal enhancement issues can be approached from a plasmonic perspective, focusing on the optimization of resonant antennae. The validity of this approach has already been confirmed by a number of studies on metal-based plasmonic geometries, [38] where substantial amplification of the local field enhancement for different geometries and arrangements of metal structures has been demonstrated. So far, the majority of works on graphene plasmonics study the effect in basic two-dimensional structures - ribbons, disks and rings. Theses structures are easily fabricated with conventional methods and altering their dimensions enable direct tunability of plasmonic resonance. Recently, the researchers turned their attention to a more complex geometries such as e.g. an array of ribbon with varying width [39], graphene disk oligomers [40], sinusoidaly-shaped patterns [41], or bi-layer structures [42]. An even stronger field enhancement and longer lifetime of plasmonic excitations compared to the basic nanoribbon arrangement has been reported in these publications. Clearly, an additional effort towards the design of graphene plasmonic antennae is required to maximize their efficiency.

According to the aforementioned, the aim of the present work is to design and fabricate a graphene-based plasmonic device to be used for the enhancement of the infrared absorption spectroscopy signal. To achieve this, at first, computational modelling of plasmonic nanoantennae is conducted and then, the experimental fabrication and characterization of graphene plasmonic chip is performed. Computational investigation focuses on maximizing the enhancement factor of plasmonic patterns based on their geometry, while the experimental section focuses mainly on fabrication process optimization. Specifically, the performance of ion-milling as graphene patterning method is investigated, addressing the issue of graphene contamination.

The paper is structured in a following way: chapter 2 gives the theoretical introduction to the topic, chapter 3 describes the methods used to collect and analyse the data in this research and the last chapter reports and discusses the results. Theoretical section introduces the necessary fundamentals of optics related to plasmonics along with basic types of plasmonic excitation. Then, applications of plasmonics will be reviewed with a particular focus on spectroscopy and sensing. The final section of theoretical chapter is dedicated to fundamental electronic, optical and plasmonic properties of graphene. This section also features the review of the latest research work on spectroscopic applications of graphene plasmonics.

2. Theory

2.1. Plasmonics

2.1.1. Free Electron gas model, volume plasmons

The theoretical background of plasmonics emerges with the attempt to describe the interaction of electromagnetic fields with conductive materials. Most of the phenomena related to plasmonics can be described by resolving only the classical theory of electromagnetism. This approach neglects the phenomena related to interaction of charged particles within matter averaging microscopic fields over significantly larger distances. Numerous books containing classical description of plasmonics have been published and this chapter is mostly based on derivations presented in Maier's "Plasmonics: Fundamentals and Applications" book [43].

A framework, known as Free Electron Gas model, is used to describe the electrons in matter responding to an external electromagnetic field. It was originally developed by Sommerfeld, and combined Fermi-Dirac statistics and Drude model of electrical conduction. The model approximates electrons with energy comparable to $k_B T$, where k_B is Boltzmann's constant and T is temperature, as a gas with number density n existing within the background of positive ion cores. The model also assumes fluid-like behavior of electrons freely-flowing inside the material, spontaneously colliding with static ion cores. Collisions occur with the average period τ, or collsion frequency $\gamma = \frac{1}{\tau}$. The equation of motion of a single electron can be written as

$$m\frac{d^2 x}{dt^2} + m\gamma\frac{dx}{dt} = -e\vec{E}, \tag{2.1}$$

where m is a the mass of electron, e is the charge of electron and $\vec{E}$ is an electric field vector. Assuming a homogeneous oscillating electric field of the form $E(t) = E_0 \exp^{-i\omega t}$, produces a solution for equation 2.1 in the form of oscillating electron motion $x(t) = x_0 \exp^{-i\omega t}$. Inserting the solution to 2.1, and solving for $x(t)$ yields the equation of electron motion

$$x(t) = \frac{e}{m(\omega^2 + i\gamma\omega)}E(t). \tag{2.2}$$

The Maxwell's Theory of Electromagnetism states the following relations for electric displacement $\vec{D} = \epsilon_0 \vec{E} + \vec{P}$ and macroscopic polarization $\vec{P} = ne\vec{x}(t)$. Combining these equations with the equation 2.2 yields the following relation

$$\vec{D} = \epsilon_0 \left(1 - \frac{\omega_p^2}{\omega^2 + i\gamma\omega} \right) \vec{E}, \tag{2.3}$$

where $\omega_p^2 = \frac{ne^2}{\epsilon_0 m}$ is a plasma frequency and $\gamma = \frac{1}{\tau}$ is the scattering rate.

The expression in brackets is a complex dielectric function. The function "encapsulates" properties of a conductive material through variables ω_p and γ, which are strongly dependant on material's microstructure. Hence, the permittivity $\epsilon(\omega)$ connects microscopic phenomena to macroscopic electromagnetic fields setting up a "phenomenological" approach for calculating the fields propagating in a conductive media. The permittivity of a material is a complex valued function of the form $\epsilon(\omega) = \epsilon_1(\omega) + i\epsilon(\omega)$. The real part ϵ_1 of dielectric function determines the amount of polarization, while imaginary part ϵ_2 is responsible for absorption. Real and imaginary components of dielectric function have the following forms

$$\epsilon_1(\omega) = 1 - \frac{\omega_p^2 \tau^2}{1 + \omega^2 \tau^2},$$

$$\tag{2.4}$$

$$\epsilon_2(\omega) = \frac{\omega_p^2 \tau}{\omega(1 + \omega^2 \tau^2)}.$$

This particular form of dielectric function, derived from Drude conductivity model, describes electromagnetic response over the range of frequencies where energy state transition occur only within the conduction band. Above a certain energy threshold, absorbed radiation will cause a transition of an electron from valence to conduction band, thus creating an electron-hole excitation. This will become a predominant factor affecting the propagation of electromagnetic waves. In order to account for the effect of inter-band transition, the equation 2.1 needs to be modified into a damped oscillator relation by adding the term $m\omega_0^2 x$, where ω_0 is the resonant frequency of the inter-band transition. Solving this equation for each allowed transition will result in the addition of Lorentz-oscillator terms, of the form $\frac{A_i}{\omega_i^2 + \omega^2 + i\gamma_i\omega}$, to the dielectric function. The region of inter-band transitions, however, is not optimal or even accessible for plasmonic application since inter-band absorption is a competing process and significant damping of plasmons are present. Therefore plasmonic response of material occurs in the region where behavior of electrons is adequately represented by the Drude model of conductivity. Dielectric function is linked to optical conductivity as

$$\epsilon(\omega) = 1 + \frac{i\sigma(\omega)}{\epsilon_0 \omega}, \qquad (2.5)$$

and to refractive index as $n = \sqrt{\epsilon}$

It is useful to analyse the dielectric function at different frequency regimes. The properties of the material, such as its ability to conduct current or electromagnetic fields can be determined by comparing real and imaginary parts of the dielectric function. For instance, if the imaginary component $\epsilon_2(\omega) \approx 0$, the material is considered to be a perfect dielectric at frequency ω, if $\frac{\epsilon_2(\omega)}{\epsilon_1(\omega)} < 1$, the material is a lossy dielectric with poor electric conductivity, at $\frac{\epsilon_2(\omega)}{\epsilon_1(\omega)} \approx 1$, the material exhibits both electrical conductance and field transmittance, if the ratio is $>> 1$ and approaching ∞, i.e. the real part is negligible, the material gains a property of perfect electrical conductor.

Dielectric function contains an important parameter, plasma frequency ω_p. In order to understand the physical meaning of the plasma frequency it is useful to remember a travelling wave solution to Maxwell's equations in Fourier space

$$\vec{k}(\vec{k} \cdot \vec{E}) - k^2 \vec{E} = -\epsilon(\vec{k}, \omega) \frac{\omega^2}{c^2} \vec{E}, \qquad (2.6)$$

where $\vec{k}$ is a wave-vector and $c = \frac{1}{\sqrt{\epsilon_0 \mu_0}}$ is the speed of light. For transverse waves with $\vec{k} \cdot \vec{E} = 0$, the equation 2.6 transforms into a dispersion relation

$$k^2 = \epsilon(\vec{k}, \omega) \frac{\omega^2}{c^2}. \qquad (2.7)$$

For longitudinal modes, however the equation 2.6 implies that $\epsilon(\vec{k}, \omega)$ must be equal to zero. If a small damping limit, $\gamma << \omega$, is considered, the dielectric function can be simplified into $\epsilon(\omega) = 1 - \frac{\omega_p}{\omega}$. Clearly, a dielectric function can only take a zero value if $\omega = \omega_p$.

The longitudinal oscillation of electron gas is demonstrated in figure 2.1. The electron density is collectively displaced by the distance u, causing the formation of surface charge density $\pm neu$ at boundaries, which lead to the appearance of homogeneous electric field $\vec{E} = \frac{neu}{\epsilon_0}$ inside the material. The displaced electron density is subjected to a restoring force. The equation of motion can be written as

$$nm\frac{d^2 u}{dt^2} = -ne\vec{E}, \qquad (2.8)$$

which, by inserting the equation for electric field, can be translated into
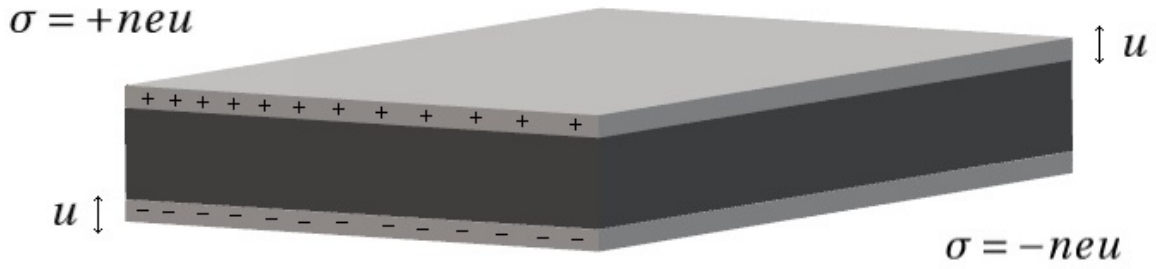
Figure 2.1: Schematic representation of collective longitudinal oscillations of electron gas (volume plasmons) in a metal slab

$$\frac{d^2 u}{d t^2} = -\frac{ne^2}{\epsilon_0 m} u = \omega_p^2 u \tag{2.9}$$

which is a form of Hooke's law for oscillating system with natural frequency ω_p. So plasma frequency is the eigenfrequency of collective longitudinal oscillation of free electron gas, also known as *bulk* or *volume* plasmon.

This type of electron density oscillation cannot couple to transverse oscillations of electromagnetic fields, and can only be induced by irradiating the material with the beam of electrons. This principle is the basis for electron energy loss spectroscopy (EELS) which can be used to determine the plasma frequency of a particular material.

2.1.2. SURFACE PLASMON POLARITONS

Surface plasmon is an oscillation of electron gas propagating along an interface between conductive and dielectric materials. Unlike volume plasmons, surface oscillations are able to couple to electromagnetic field in a form of *surface plasmon polaritons (SPP)* - a hybrid between electromagnetic and electron density waves propagating in the surface plane and highly confined in the perpendicular direction.

The description of propagating electromagnetic waves starts with the wave equation

$$\nabla^2 \vec{E} = \frac{\epsilon}{c^2} \frac{\partial^2 \vec{E}}{\partial t^2}, \tag{2.10}$$

which, assuming a harmonic time dependence of the electric field, $\vec{E}(\vec{r}, t) = \vec{E}(r)e^{-i\omega t}$ is transformed into *Helmholtz equation*

$$\nabla^2 \vec{E} = -k_0^2 \epsilon \vec{E}, \tag{2.11}$$

where $k_0 = \frac{\omega}{c}$. For simplicity, the propagation of the wave can be restricted to a single direction, x, assuming $x - y$-plane to be the parallel to the metal-dielectric interface positioned at $z = 0$. The propagating wave can be described as $\vec{E}(x, y, z) = E(z)e^{ik_x x}$ where k_x is a wave vector in the direction of propagation. In order to find dispersion relation of surface electromagnetic waves, the curl equations $\nabla \times \vec{E} = \mu_0 \frac{\partial \vec{H}}{\partial t}$ and $\nabla \times \vec{H} = \epsilon_0 \epsilon \frac{\partial \vec{E}}{\partial t}$ need to be solved for each field components for cases of transverse magnetic (E_x, E_z, H_y are nonzero), and transverse electric (H_x, H_z, E_y are nonzero) wave polarisations. Taking into account continuity of fields across the interface, surface modes exist only for transverse magnetic (TM) polarisation. A complete derivation of field components can be found in Maier's [43].

The result of mathematical description of surface plasmons is the dispersion relation between angular frequency ω and propagation vector k such as

$$k_x(\omega) = \sqrt{\frac{\epsilon_1(\omega)\epsilon_2}{\epsilon_1(\omega) + \epsilon_2}}, \tag{2.12}$$

where $\epsilon_1(\omega)$ is a frequency dependent permittivity of the metal and ϵ_2 is a permittivity of the dielectric. This dispersion relation along with 2.7 are plotted in the figure 2.2. There are two distinctive regimes observed in the surface plasmon dispersion. At low k_x, the dispersion is close to the dispersion of light and surface plasmon polaritons have propagating characteristics. This regime is also known as "Zommerfeld-Zennek" waves. As k_x diverges, the frequency approaches a limit at the characteristic frequency of surface plasmon $\omega_{sp} = \frac{\omega_p}{\sqrt{1+\epsilon_2}}$. In this regime the group velocity $\frac{\partial \omega}{\partial k_x}$, wavelength $\lambda = \frac{1}{k_x}$ and decay length in z-direction $k_z = \frac{1}{\sqrt{k_x^2 - \epsilon_2(\frac{\omega}{c})}}$ approach zero, meaning that surface plasmon tend to become electrostatic. This regime is characterized by high confinement of light and is sometimes referred to as Fano mode [44].At frequencies above $\frac{\omega}{\omega_p} > 1$ resides the so-called Brewster regime [45], and the material becomes transparent. The dispersion model is based on the assumption of negligible (zero) damping, thus there is a "forbidden gap" between ω_{sp} and ω_p However, in case of real material, the losses needs to be taken into account. In this case, the wave vector becomes complex and is not anymore diverging to infinity. Instead, due to contribution of relaxation and inter-band transitions, it curves backwards connecting surface plasmon and Brewster modes. This regime, named quasi-static, demonstrates an unusual behaviors such as negative group velocity.

SPP is excited by an incident radiation that induces polarization in the material resulting in the oscillation of electron density coupled to an electromagnetic field. The magnitude of the evanescent field decays exponentially away from the interface in z-direction. The schematics of this process is shown in the figure 2.3. It should be noted that the incident radiation is not able to excite SPP directly since the wave vector of the surface plasmon
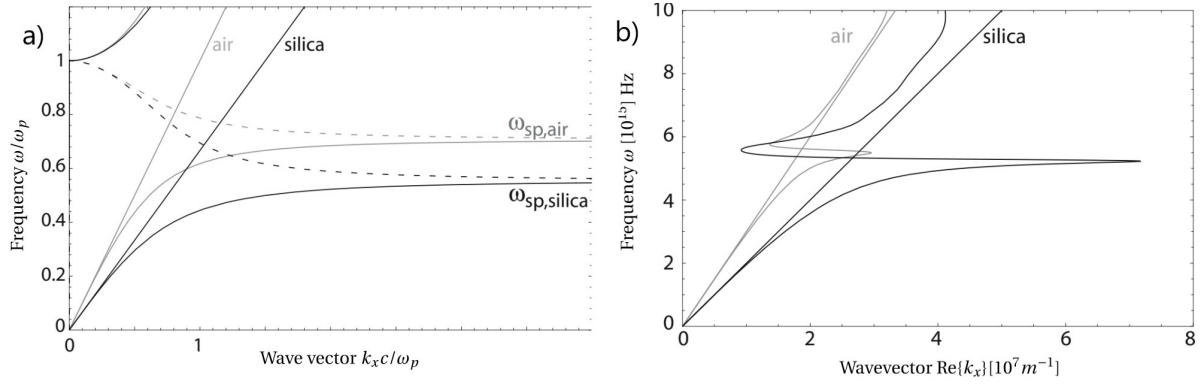
Figure 2.2: a) Dispersion relation of surface plasmons and volume plasma oscillation for metal/air (gray curve) and metal/silica (black curve) interfaces. The dashed line represent the imaginary component of wave vector. b) Dispersion relation of silver/air(gray) silver/silica (black) interfaces based on the experimental complex refractive index data [43], [46]

is always greater than the wave vector of light propagating through dielectric. There is a variety of methods to overcome the mismatch. The earliest techniques, proposed by Otto and Kretschmann, involve a prism with high refractive index compared to interface dielectric. The light, entering the prism under the angle greater than total internal reflection threshold angle, causes the evanescent waves to expand out of the prism's interface. In the Kretschmann method, the metal film is in direct contact with the prism so the evanescent field tunnels through it, while Otto's method suggests placing the prism at a distance to the metal interface leaving a gap where the excitation occurs. Alternatively, a grating coupling can be used for phase-matching between incident light and the surface plasmons. The grating, with constant a (spacing between groves), can be fabricated directly on the metal surface enabling plasmon excitation upon matching $k_x = k \sin \theta + g \frac{2\pi}{a}$ where g is a positive integer indicating the grating order. The grating also allows backward process - "decoupling" of surface plasmons polaritons into outgoing radiation. Generally any sufficiently rough surface can be considered as a grating. Another method, proposed by Bouhelier and Wiederrecht [47], utilizes a microscope with an immersion objective and high numerical aperture lens to excite SPP modes in glass/metal interface. Lastly, SPP can be launched via direct near-field excitation. The set-up is similar to scanning probe systems but uses an optical fiber instead of a cantilever to probe the electric field within the decay length of plasmon modes. This instrument is called scanning near-field optical microscope (SNOM).
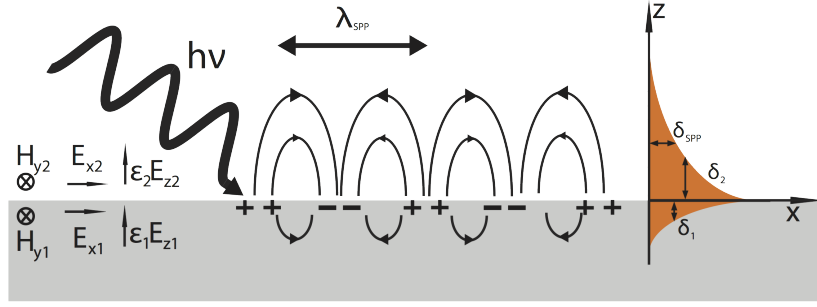
Figure 2.3: Schematic representation of the surface plasmon polariton [48]

2.1.3. LOCALIZED SURFACE PLASMONS

The third fundamental type of plasmonic excitations is *localised surface plasmon (LSP)* which occurs in metallic nanostructures or nanoparticles with dimensions smaller than the wavelength of the incident light. Upon irradiation, the electron density inside a particle begins to fluctuate, so the particle behaves as an oscillating dipole surrounded by the surface-confined electromagnetic field. Schematically, the phenomenon is illustrated in the figure 2.4.
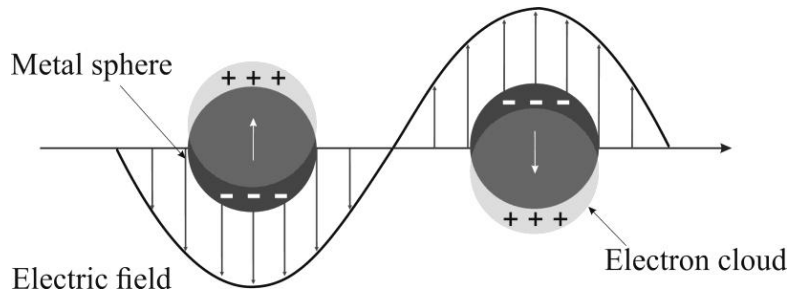

Figure 2.4: Schematic representation of a dipole surface plasmon confined to a spherical nanoparticle [49]

To describe localized surface plasmon resonance, a simple object, such as a sphere, with radius *a*, placed inside a static potential is to be considered. The justification of viewing this problem as an electrostatic is the condition $a \ll \lambda_{light}$, meaning that at any moment in time each point of a sphere experience nearly the same phase of the incident wave. The electric field in this case is a negative gradient of scalar potential function Φ, which can be found by solving a Laplace equation $\nabla^2\Phi = 0$. The solution for the case of spherical nanoparticle are derived in Jacksons's book[50]. Applying boundary conditions of equality of tangential components of magnetic field and normal components of electric field at the boundary of nanosphere with permittivity ϵ placed in dielectric medium, with constant

permittivity ϵ_m, leads to the solutions for the potential Φ_{in} inside and Φ_{out} outside the sphere in the form

$$\Phi_{in} = -\frac{3\epsilon_m}{\epsilon + 2\epsilon_m} E_0 r \cos\theta, \tag{2.13}$$

$$\Phi_{out} = -E_0 r \cos\theta + \frac{\epsilon - \epsilon_m}{\epsilon + 2\epsilon_m} E_0 a^3 \frac{\cos\theta}{r^2}, \tag{2.14}$$

where r is the vector originating in the center of the sphere and pointing outwards with the angle θ to the direction of static electric field with amplitude E_0. Physically Φ_{out} describes the sum of the applied electric field and the one generated by a dipole in the center of the sphere, therefore Φ_{in} can be ignored. The equation 2.14 can be rewritten in terms of dipole moment $\vec{p} = 4\pi\epsilon_0\epsilon_m a^3 \frac{\epsilon - \epsilon_m}{\epsilon + 2\epsilon_m} \vec{E}_0$ as

$$\Phi_{out} = -E_0 r \cos\theta + \frac{\vec{p} \cdot \vec{r}}{4\pi\epsilon_0\epsilon_m r^3}, \tag{2.15}$$

and taking into account that $\vec{p} = \epsilon_0\epsilon_m \alpha \vec{E}_0$ allows to introduce polarizability term α which for the case of spherical particle is described as

$$\alpha = 4\pi a^3 \frac{\epsilon - \epsilon_m}{\epsilon + 2\epsilon_m}. \tag{2.16}$$

Polarizability describes the resonant condition of a nanosphere. It is evident that polarizability aproaches it's maximum value at $Re\{\epsilon(\omega)\} = -2\epsilon_m$, which is known as the Fröhlich condition. The resulting distribution of the potential, calculated from the equation 2.15, represents a dipole surface oscillation, which is the fundamental resonance mode of the localized surface plasmon. Polarizability also increases the efficiency of scattering and absorption of light by a nanoparticle, this can be observed from corresponding (C_{scat}) and (C_{abs}) cross-sections

$$C_{scat} = \frac{k^4}{6\pi} |\alpha|^2, \tag{2.17}$$

$$C_{abs} = k Im\{\alpha\}, \tag{2.18}$$

which show that the size variation affect both phenomena at a different rate. In the case of scattering, the scaling is $\propto a^6$, while the absorbtion cross-section is proportional to a third power of particle's radius. This indicates that for a larger nanoparticles, the scattering is a dominating process. In a more general case of ellipsoid, described by three radii a_1, a_2 and a_3 the expression of polarizability along each axis $i = 1, 2, 3$ is extended to

$$\alpha_i = 4\pi a_1 a_2 a_3 \frac{\epsilon(\omega) - \epsilon_m}{3\epsilon_m + 3L_i(\epsilon(\omega) - \epsilon_m)}, \tag{2.19}$$

where L_i is geometrical factor dependent on a_i full description of which can be found in the Maier's book.[43]

Adding a harmonic time dependence $e^{-i\omega t}$ to the incident wave, particle starts to behave like an oscillating dipole with moment $\vec{p} = \epsilon_0 \epsilon_m \alpha \vec{E}_0 e^{-i\omega t}$. The expression for total electric and magnetic fields of oscillating dipole are

$$\vec{E}(t) = \frac{1}{4\pi\epsilon_0\epsilon_m} \left[k^2 (\vec{n} \times \vec{p}) \times \vec{n} \frac{e^{ikr}}{r} + (3\vec{n}(\vec{n} \cdot \vec{p}) - \vec{p}) \left(\frac{1}{r^3} - \frac{ik}{r^2} \right) e^{ikr} \right] e^{-i\omega t} \qquad (2.20)$$

and

$$\vec{H}(t) = \left[\frac{ck^2}{4\pi} (\vec{n} \times \vec{p}) \frac{e^{ikr}}{r} \left(1 - \frac{1}{ikr} \right) \right] e^{-i\omega t}, \qquad (2.21)$$

where $\vec{n}$ is a unit vector originating in the center of the sphere and pointing in a random direction. The near-field and far-field distributions can be extracted from these equations by considering limits $kr \ll 1$ and $kr \gg 1$ respectively. The resulting distribution of electric field for both conditions for a spheroid are presented in the figure 2.5
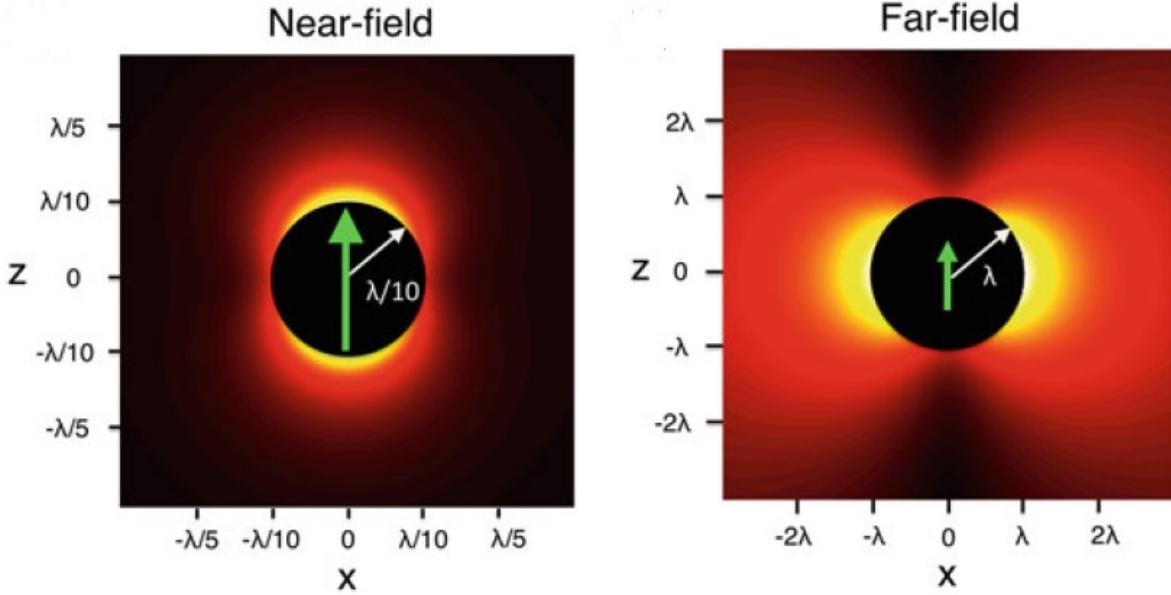

Figure 2.5: Computationally modeled modulus of the electric near-field and far-field distribution around the spherical nanoparticle induced by the plasmonic excitation.[51]

Quazi-static approach, described above, is valid for nanoparticles with diameter in the range of 10 to 100 nm. At the lower limit, the mean free path of electrons becomes substantially smaller than the mean free path in bulk material, hence the the damping of the density oscillation occurs at the interface of the nanoparticle. This causes the damping rate to increase and decay time of LSP to decrease. This can be observed as a broadening

of linewidth of plasmon spectrum. At the upper limit of a particle radius, a simple quasi-static approximation looses its validity as the size of the sphere approaches the wavelength of incident radiation and the phase difference over particle volume becomes significant. A rigorous theory describing scattering and absorption of light by spherical particles was developed by Mie [9], and is known as *Mie theory*. The theory classifies scattered and internal fields into a series of normal modes. Using this theory the the polarizability of a sphere can be represented as a power expansion of the first transverse-magnetic mode

$$\alpha = \frac{1 - (\frac{1}{10})(\epsilon + \epsilon_m)x^2 + O(x^4)}{(\frac{1}{3} + \frac{\epsilon_m}{\epsilon - \epsilon_m}) - \frac{1}{30}(\epsilon + 10\epsilon_m)x^2 - i\frac{4\pi^2\epsilon_m^{3/2}}{3}\frac{V}{\lambda_0^3} + O(x^4)}V, \tag{2.22}$$

where V is the volume of a sphere, $x = \frac{\pi a}{\lambda}$ and O represents higher order terms. Quadratic terms in this equation correspond to the degradation of the excitation and depolarization field, while the imaginary term is related to the lifetime of the resonance. The damping of LSP excitation is governed by radiative process (photon emission), dominating for larger particles, as well as a non-radiative absorption. Localized plasmon modes of neighbour particles are able to couple between each other forming a chain of collectively oscillating dipoles. Two types of coupling must be distinguished - near-field coupling occurring when the separation distance $d \ll \lambda_0$ and far-field interaction, when the spacing between nanoparticles is comparable to the wavelength and larger. In the first case, the interaction strength scales with d^{-3}. At close distances the far-field scattering process is suppressed by a neighbouring particles, exhibiting a chain excitation of localized plasmons. This leads to large enhancement of the electric field in the gap between nanoparticles. These hot spots are are used to amplify photon-driven processes, such as Raman scattering, radiation absorption and fluorescence. The distance between particles also affects the resonance frequency. As depicted in the figure 2.6, depending on a polarization, the frequency can either blue-shift (transverse modes) or red-shift (longitudinal modes) as the spacing between particles shrinks. At longitudinal polarization, the chain of nanoparticles can transmit the excitation to the neighbour particles, thus acting as a waveguide.

As the separation distance approaches the excitation wavelength, the near-field coupling looses its effect, and far-field dipolar coupling starts to dominate. In this regime the coupling strength is proportional to $\frac{1}{d}$, and the variation of the distance mostly affects the linewidth (decay rate) of the resonance. The effect of separation distance (grating constant) between nanoparticles in the array is illustrated in the figure 2.7. At a certain distance, the grating resonance has the greatest effect resulting in the narrowest observed linewidth. The variation of distance also affects the position of the peak, albeit less drastically than in the case of the near-field coupling.
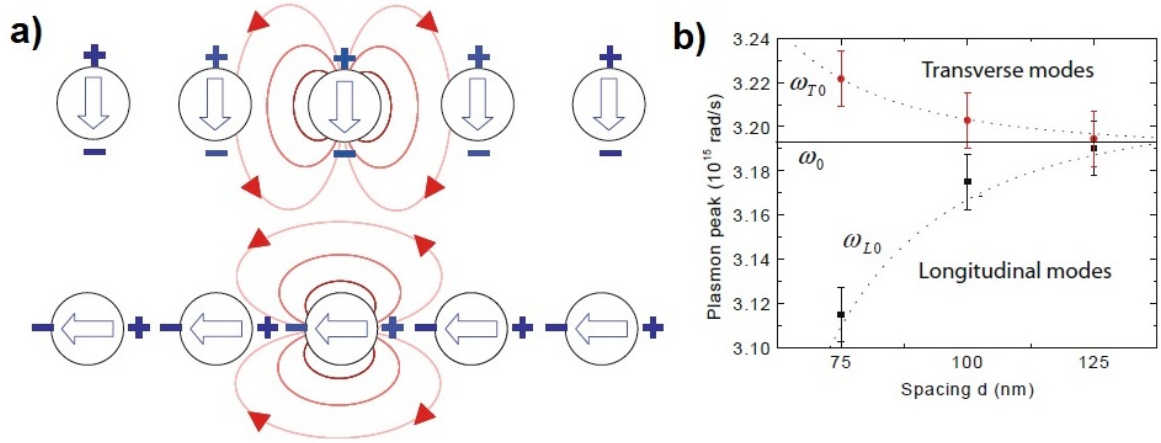
Figure 2.6: a) Schematic representation of near-field coupling with transverse (top) and longitudinal (bottom) polarization [43] b) Dependence of the plasmonic resonance frequency on separation distance for both polarization modes [52]

Another type of localised plasmon resonance are called void plasmons. The case of void plasmons is similar to the one of nanoparticles, except the dielectric and metal "swapped" places. In practice, void plasmons are supported by nanoholes, cavities and dielectric inclusions into a bulk metal. The polarizability of a spherical void is similar to the one of a nanosphere (eq. 2.16), but the permittivities of medium and material are switched. The Fröhlich condition in this case is $Re(\epsilon(\omega)) = -\frac{1}{2}\epsilon_m$.

2.2. APPLICATION OF PLASMONICS FOR SURFACE ENHANCED SPECTROSCOPIES AND SENSING

2.2.1. PLASMONIC-BASED REFRACTIVE INDEX SENSOR

Among the others, spectroscopy and sensing are the most prominent applications of plasmonics. Being based on a single phenomena, these application exploit different aspects of it. Plasmonic sensors are based on the far-field emitted signal, while spectroscopic applications rely on the enhancement of light-matter interaction rates occurring in the near-field. Sensing utilizes a straightforward approach: both surface plasmon polartons (equation 2.12) and localized modes (equation 2.16) are sensitive to the variation of the refractive index of surrounding media, expressed as a shift in the observed signal. Sufficient change in the concentration of dissolved molecules alters the effective refractive index of a surrounding medium which can be used to detect any changes in the local chemical composition.
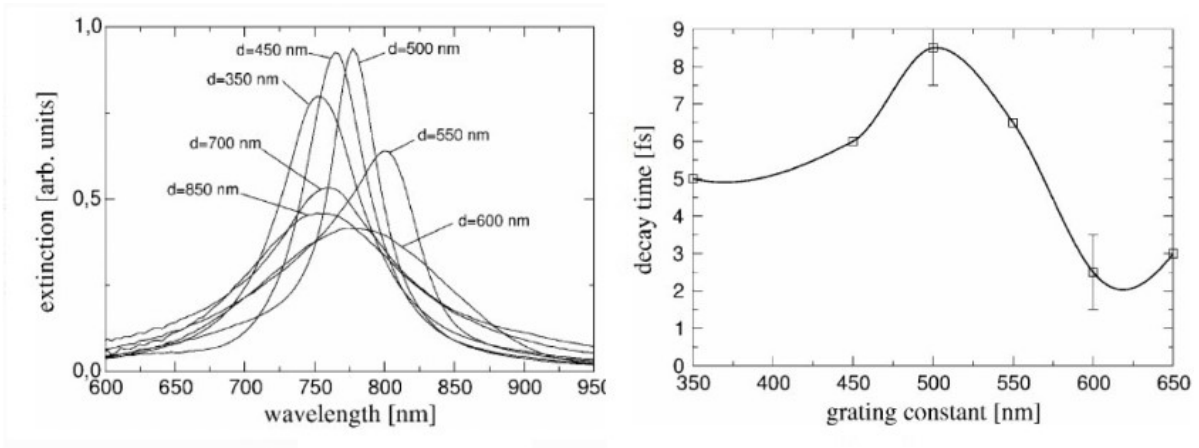
Figure 2.7: Effect of the separation distance for far-field coupled nanoparticles. a) Observed variation of extinction spectra for different grating constant. b) Variation of the decay rate (linewidth) with increasing separation distance [53]

The example of the setup and observed spectral shift is illustrated in the figure 2.8. Because of the tight confinement of electromagnetic field to the surface of plasmonic antenna, the resonance is particularly sensitive to a directly adsorbed monolayer of analyte. Therefore, in order to increase the sensitivity, a surface, containing plasmonic species, must be functionalized to ensure a selective molecular adsorption. For general sensing applications only radiative far-field is responsible for an observed signal, therefore the separation between plasmonic structures must ensure the condition for the strongest far-field coupling. This approach has been well developed and is widely used for analysis of biological samples. Some of the notable examples of plasmonic sensor, based on refractive index change are presented in a number of publications [54]–[57].

2.2.2. PURCELL EFFECT

For spectroscopic applications, the key idea is to use plasmon resonance to increase the rate of light-matter interaction events, resulting in an enhancement of the observed signal. The underlying physics of optical spectroscopy is based around the emission or absorption of photons by a molecule. This process can be viewed as a series of transitions between electronic states occurring with a specific probability. The transition probability W of randomly oriented dipole is expressed by Fermi's golden rule as:

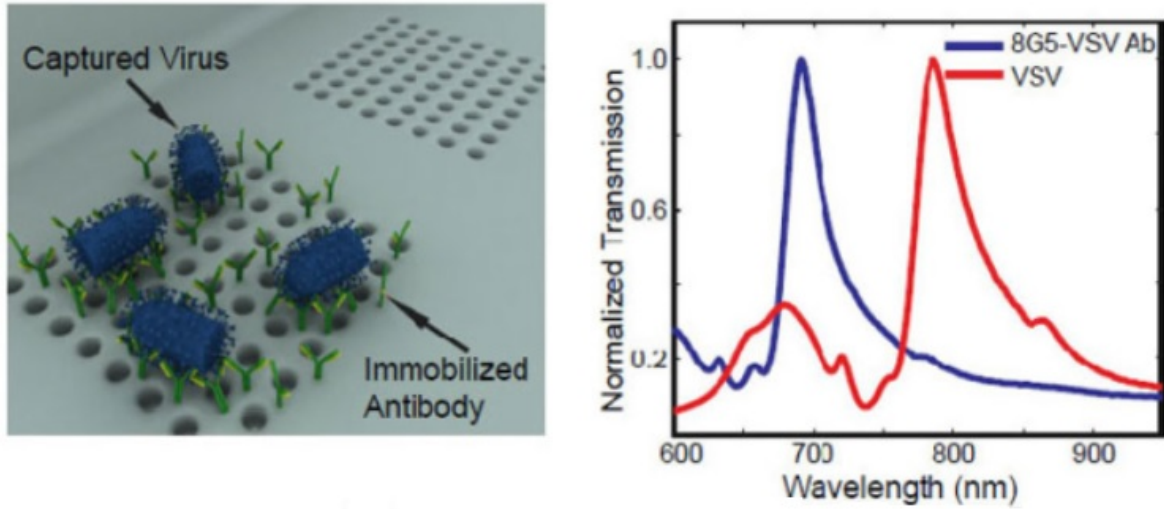$$W = \frac{2\pi}{3\hbar} |p \cdot E|^2 g(\omega), \tag{2.23}$$

15

Figure 2.8: The design of plasmonic sensor based on the array of nanoholes for sensing of viruses(left picture) and the experimental spectral data (right picture). Red curve is the transmission spectrum with adsorbed virus species, blue curve is the spectrum of the reference array.[58]

where p is transition dipole moment and $g(\omega)$ is the density of optical modes[59]. So the total rate is directly proportional to the intensity of the electric field and mode density. Any resonant cavity, that is able to sustains confined light modes, can affect the transition rate via alteration of theses parameters. An enhancement of spontaneous emission by a resonant optical cavity is called the *Purcell effect*. The enhancement factor can be expressed as $F = \frac{W_{cavity}}{W_{free}}$, a ratio between transition probability inside a cavity and in a free space. Directly from the equation 2.23 it can be assumed that

$$F = \frac{|E_{loc}(\omega)|^2}{|E_{free}(\omega)|^2},$$ (2.24)

where $E_{loc}(\omega)$ is the resulting magnitude of the electric field in the optical cavity and $E_{free}(\omega)$ is the magnitude of the electric field in a free space [59].The equation 2.23 can be further specified for a free space and a cavity environments by defining the corresponding mode densities $g(\omega)$ as

16

$$g_{free}(\omega) = \frac{\omega^2 V}{\pi c^3}$$

(2.25)

$$g_{cav}(\omega) = \frac{2}{\pi} \frac{\Delta\omega_{cav}}{4(\omega - \omega_{cav})^2 + \Delta\omega_{cav}^2}$$

respectively, where $\Delta\omega_{cav}$ is the line-width of a resonator. Assuming the amplitude of the zero-point energy electric field in the volume V of space (V_c in the case of optical cavity) as $|E| = \sqrt{\frac{\hbar\omega}{2\epsilon_0 V}}$, the Purcell enhancement factor at the resonant frequency is then defined as

$$F = \frac{3Q(\lambda/n^3)}{4\pi V_c}$$

(2.26)

where λ is a wavelength of free space, n is the refractive index inside the cavity and $Q = \frac{\omega_{cav}}{\Delta\omega_{cav}}$ is quality factor of a resonant optical cavity [59]. The equation 2.26 represents the enhancement factor of the optical environment in terms of temporal Q and spatial $(\lambda/n^3)/V_c$ contributions and is a more comprehensive definition to be used in the design of optical resonators. The general definition shown in the equation 2.24 takes into account the resulting field intensity and is equally valid.

2.2.3. SURFACE ENHANCED RAMAN SCATTERING

Based on the source, two mutually compatible approaches to the enhanced Raman spectroscopy have been developed - *Tip-Enhanced Raman Spectroscopy (TERS)* and *Surface-Enhanced Raman Spectroscopy (SERS)*. Both of these techniques rely on the Purcell effect produced by the LSP modes sustained at the nanostructured surface or metallized tip with extremely sharp apex. Analyte molecules, which are placed inside the near-field, display the enhancement of Raman signal if plasmonic resonance of surface structures or a tip are in tune with the probing radiation.

Fundamentally, Raman spectroscopy is based on the phenomenon of inelastic scattering of electromagnetic radiation by molecules due to excitation or relaxation of vibrational or rotational motions. As it is seen in the figure 2.9, Raman scattering is a two photon process - excitation photon, with frequency ν_L, can either undergo Stokes or an anti-Stokes scattering. In the former case the frequency ν_S of emitted photon decreases, while in the latter case, the frequency ν_{aS} increases, by the difference ν_M, which corresponds to the characteristic vibrational frequency of a molecule. Taking into account selection rules for vibrations transitions, masses and bond lengths of constituent chemical moieties can be deduced from the observed shift.
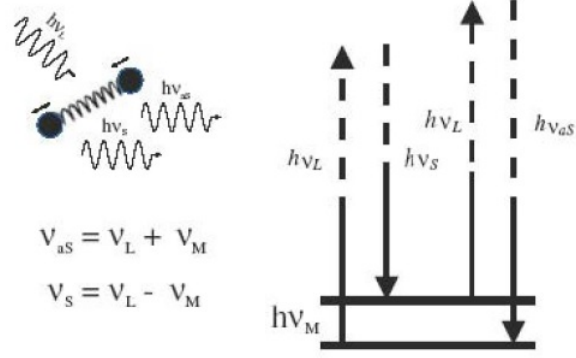
17

Figure 2.9: Illustration of Raman scattering process with energy transition diagram for Stokes and Anti-Stokes scattering events [43]

.

An enhancement factor P_{SERS} for Raman scattering can be represented in terms of electromagnetic and chemical contributions of surrounding environment as

$$P_{SERS}(\nu_S) = N\sigma_{scat}F(\nu_L)F(\nu_S)I(\nu_L), \qquad (2.27)$$

where N is the number of active species in an enhanced area, $F(\nu) = \frac{|E_{loc}|^2}{|E_0|^2}$ is the electromagnetic enhancement factor, and I is the intensity of an incident beam. The term σ_{scat} is a scattering cross section of active species in an enhanced region. According to Sharma et al. [38], the scattering cross section can be increased up to 4 orders of magnitude via chemical pathway. A typical scattering cross section is of the order 10^{-30} cm^2/molecule. It should be noted that the electromagnetic enhancement F affects both incoming and scattered radiation. Typically the difference ν_M is smaller than the linewidth of plasmonic resonance meaning that the total electromagnetic enhancement factor is F^2 which translates into rather significant numbers in the order of 10^{10} in hot spot areas [38]. The electromagnetic contribution to the enhancement factor can be further expressed as

$$F(\nu) = L_{SP}(\nu)L_{LR}, \qquad (2.28)$$

where L_{SP} is contribution of localised plasmonic excitation, and L_{LR} is contribution factor of "lightning rod" effect, caused by a rapid variations of potential in the vicinity of a curved surface and is attributed to sharp features with low curvature radius in the geometry of plasmonic structure.

2.2.4. SURFACE-ENHANCED INFRARED ABSORPTION

A complimentary, to Raman scattering, technique is the *Surface-Enhanced IR Absorption* (SEIRA) spectroscopy. Infrared spectroscopy is based on the phenomenon of absorption of probing radiation by molecules. Similarly to the Raman scattering, the absorption of radiation is due to excitation characteristic vibraional modes. Selection rules for transitions are similar, but not exaclty the same, to Raman producing similar spectral data. The principal differences are the spectral range of probing radiation and the single-photon nature of the absorption process. Hence, the enhancement factor is

$$P_{SEIRA}(\nu) = F(\nu)\sigma_{abs}I(\nu), \tag{2.29}$$

where σ_{abs} is the absorption cross section and $F(\nu)$ is the Purcell factor. Unlike in SERS, the electromagnetic amplification in SEIRA is only F, therefore a stronger emphasis should be made on the design of plasmonic antennas with sufficiently high local field enhancement factor and high density of active hot spots to achieve sufficient enhancement of SEIRA signal. A variety of research papers on plasmonic geometries have been published. A spectral characteristics and the field enhancement were studied for variety of structures including basic primitives such as nanorods [60], nanodiscs [61], and cubic nanoparticles [62], as well as a more complex structures such as nanorice [63], nanostar [64], nanoshells and cups [65], and spirals [66]. The figure 2.10 presents some of the most prominent experimental results for rod [60], bar [67] and cross-shaped [68] antennae. Reported enhancement factor achieved with these geometries is in the range of $10^3 - 10^5$. The spectral range covered with metallic antennas resides within 3000 - 1000 cm^{-1}, which is well sufficient for most of the IR measurements, however leaving out the far-IR infrared range 500-1000 cm^{-1}, where characteristic frequencies of e.g., halogeno-organic moieties are present. In order to reach these frequencies, the structure must be elongated more than several microns while the active SEIRA region remains the same. That means that the areal density of hot spots is significantly lower than in the case of SERS resonant antennas where critical dimensions are in the nanometer range.

SUMMARY

Previous sections reviewed the topic of plasmonics from the phenomenological viewpoint of classical Maxwell's theory of electromagnetism. Microscopic light-matter interactions in a medium are averaged into a dielectric function that accounts for polarzation and losses in a material and dictates how the light behaves in it. Metals and other conductive materials, for that matter, are the special case since their outer-shell electrons are delocalized inside
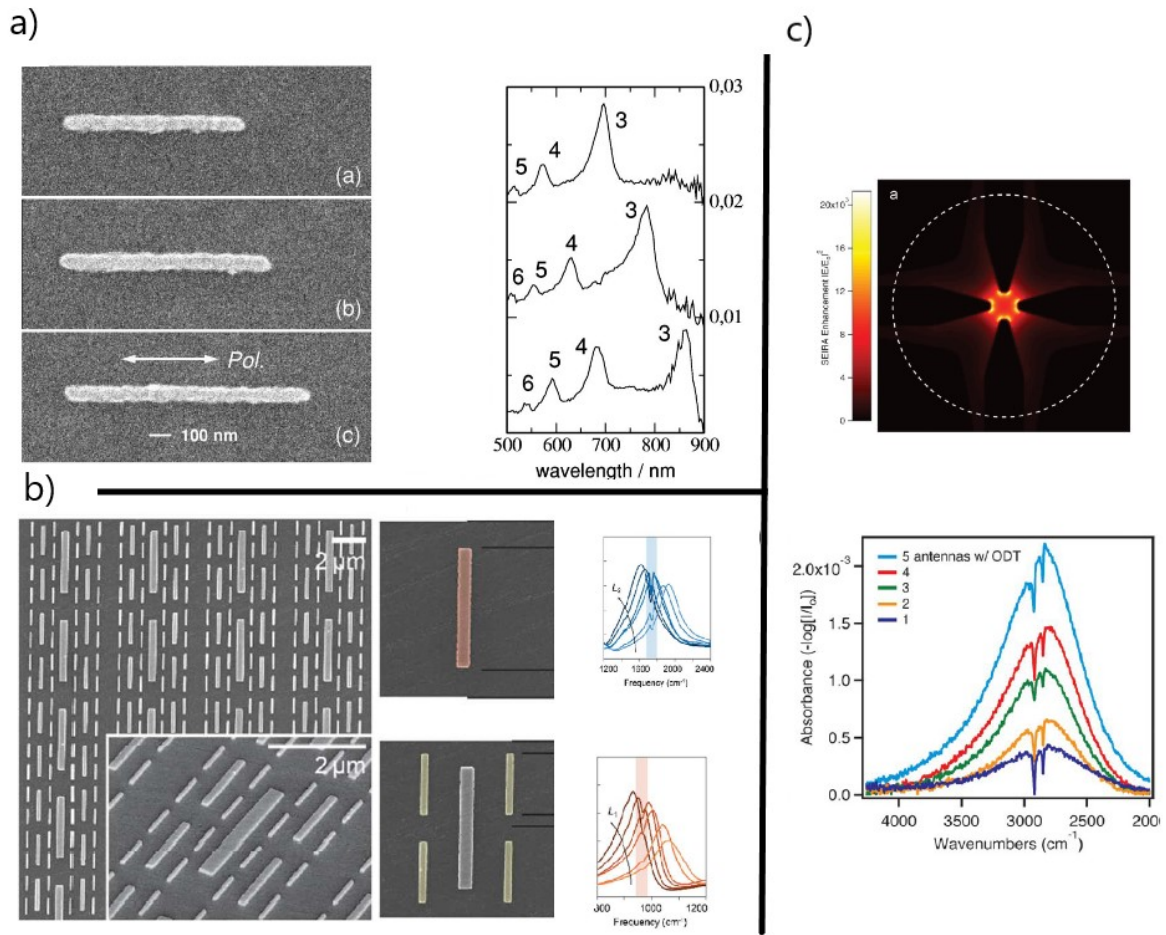
Figure 2.10: a) Scanning Electron Microscope image and the corresponding absorption spectrum of nanorods with different length b) SEM images of nanobar multi array, and absorbtion spectrum of nanobars with two different sizes c) Simulated electromagnetic field profile (modulus squared) of the "cross" arrangement and corresponding SEIRA spectrum of octadecanethiol (ODT). Only the hot spot area is demonstrated, the length of each ray of the cross is $\approx 1\mu m$

the crystal structure and can be approximately viewed as gas of charged particles (plasma). The density of the electron gas may change over the volume in response to external factors. Harmonic oscillation of electron gas are called plasmons. There are three fundamental type of plasmons: bulk, surface and localized. Bulk plasmons are longitudinal oscillation inside the metal, that are not able to couple to external electromagnetic field, whereas SPP and LSP are. Surface plasmon polaritons are collective oscillation at the flat metal dielectric interface and can propagate along it. Localized surface plasmon modes are supported around microscopic metallic structures behaving as oscillating dipoles. Both types are

characterized by the high confinement of electromagnetic field below the diffraction limit. High field confinement around nanostructures result in the large enhancement of the electromagnetic field magnitude, which exponentially decays away from the interface. Field amplification enables the enhancement of photon-driven processes such as molecular absorption, scattering and fluorescence. Surface-enhanced infrared absorption spectroscopy has proven its viability, demonstrating an enhancement factors of $\approx 10^4$. However typical plasmonic materials, noble-metals, require a high aspect-ratio structures to reach the required spectral range with plasmonic resonance, making the structures bulky in comparison to microscopic hot spots. Therefore, other materials possessing plasmonic properties at Far-IR range and larger confinement factor need to be investigated. The next chapters will introduce graphene as plasmonic material with intriguing properties that can fulfill the requirements for SEIRA.

2.3.1. STRUCTURE AND ELECTRONIC PROPERTIES

This chapter will introduce graphene and its electronic and optical properties. Graphene is a structural allotrope of carbon, a single monolayer of graphite. Carbon atoms in graphene are oriented in a hexagonal pattern as presented in the figure 2.11. The outer shell electronic structure of carbon atom consists of 3 sp^2-hybridized orbitals that constitute a chemical bonding to three neighboring atoms. The bond length, a_0, is equal to 1.42Å. The remaining electron cloud is oriented perpendicularly to the crystal plane, forming $2p_z$ orbital. Neighbouring $2p_z$ orbitals overlaps with hopping integral $t = -2.7eV$, enabling mobility of electrons across the entire graphene crystal. Naturally, these electrons are responsible for electronic and optical properties of graphene.
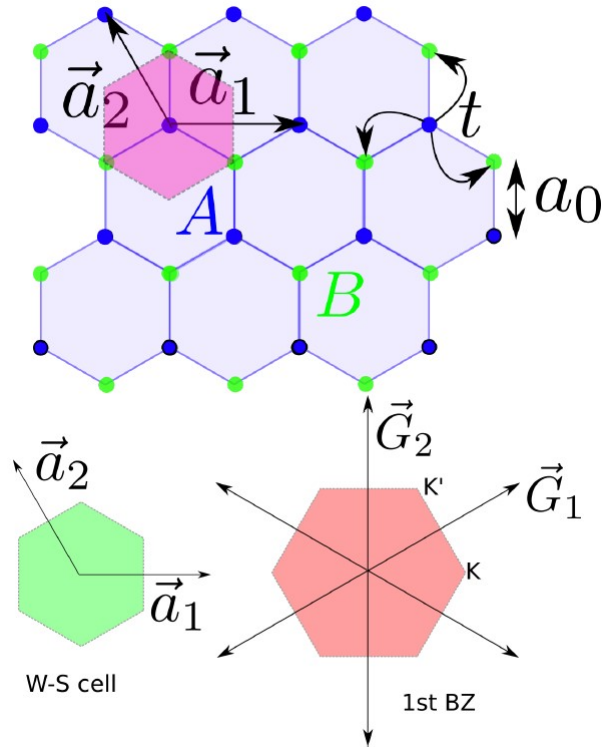

Figure 2.11: Top: real-space crystal structure of graphene. Bottom: Wigner-Seitz cell (green) and the first Brillouin zone of momentum space (red) with corresponding lattice vectors

The mathematical description of these properties starts with the definition of real and reciprocal spatial structures of graphene sheet (figure 2.11). The lattice vectors a_1 and a_2

can be described in terms of atomic spacing, a_0, as

$$a_1 = a_0(\sqrt{3}, 0),$$
$$a_2 = a_0(-\frac{\sqrt{3}}{2}, \frac{1}{2}),$$

(2.30)

and corresponding reciprocal space vectors are described as

$$G_1 = (\frac{\sqrt{3}}{2}, \frac{1}{2}),$$
$$G_2 = \frac{4\pi}{a_0}(0, 1).$$

(2.31)

Points K and K´, named Dirac points, correspond to direction along zig-zag edges pointing outwards each atom in the real space [23]. The starting point for the derivation of the optical properties of graphene is the description of its electronic band structure. First of all, since only p_z orbitals are considered, the Hamiltonian of the system consisting of a localized atomic orbitals of carbon atom and 3 nearest neighbors is expressed as

$$H = t \sum_R \{|A, \mathbf{R}\rangle [\langle B, \mathbf{R} + \delta_1| + \langle B, \mathbf{R} + \delta_2| + \langle B, \mathbf{R} + \delta_3|] + H.C.\},$$

(2.32)

where $|A, \mathbf{R}\rangle$ is the localized molecular orbital of the atom in sub-lattice A (see figure 2.11), $\langle B, \mathbf{B} + \delta_i|$ are orbitals of atoms ($i = 1, 2, 3$) located in sub-lattice B, H.C. is Hermitian Conjugate and $\mathbf{R}$ and $\mathbf{R} + \delta_i$ are position vectors of corresponding atoms. In terms of Bloch states, the Hamiltonian is expressed as

$$H = t \sum_k \{|A, \mathbf{k}\rangle \langle B, \mathbf{k}|\phi(\mathbf{k}) + H.C.\},$$

(2.33)

where $\mathbf{k} = (k_x, k_y)$ is a wave vector of Bloch wave and t is the overlap integral mentioned before. The wavefunction $\phi(\mathbf{k})$ is defined as

$$\phi(\mathbf{k}) = e^{ik_y a_0} + e^{ik_x \sqrt{3} a_0/2} e^{-ik_y a_0/2} + e^{-ik_x \sqrt{3} a_0/2} e^{-ik_y a_0/2}.$$

(2.34)

The Hamiltonian operator of the equation 2.33 can be rewritten in the matrix form as

$$H_k = \begin{bmatrix} 0 & t\phi(\mathbf{k}) \\ t\phi^*(\mathbf{k}) & 0 \end{bmatrix}$$

(2.35)

and the resulting energy spectrum is

$$E_k = \pm t|\phi(\mathbf{k})| = \pm t \sqrt{3 + 2\cos\sqrt{3}k_x a_0 + 4\cos\frac{\sqrt{3}}{2}k_x a_0 \cos\frac{3}{2}k_y a_0}.$$

(2.36)

It can be seen form the equation 2.36, that the band structure consists of two symmetrical bands, filled valence band with energy $-t|\phi(\mathbf{k})|$ and empty conduction band $t|\phi(\mathbf{k})|$ [69]. Plotting the result (figure 2.12) reveals a peculiar features of the band diagram: valence and conduction bands "meet" around K and K' points having a zero band gap. Moreover, low energy band structure around Dirac points is shaped conically, which means that the dispersion is linear in this region. To support this idea mathematically, Hamiltonian should be re-written in terms of vector $\mathbf{q}$, which is a difference between wave vector $\mathbf{k}$ and Dirac point wave vector $\mathbf{K}$, in the limit of $\frac{\mathbf{q}}{\mathbf{K}} \ll 1$. The low-energy Hamiltonian is the represented as

$$H = \frac{3}{2} a_0 t \begin{bmatrix} 0 & i\partial_x + \partial_y \\ i\partial_x - \partial_y & \end{bmatrix},$$
(2.37)

which is a a Hamiltonian of massless Dirac fermions with energy eigenvalues

$$E_\pm(\mathbf{q}) = \pm \hbar v_f q,$$
(2.38)

where $v_f \approx c/300$ is a Fermi velocity and $\hbar$ is Plank's constant [69]. The dispersion of electron energies linearly scales with momentum in the vicinity of K points which supports the observation. In turn, q can be related to a carrier concentration as $q = \sqrt{\pi n}$ where n is the number of additional charge carriers [27].
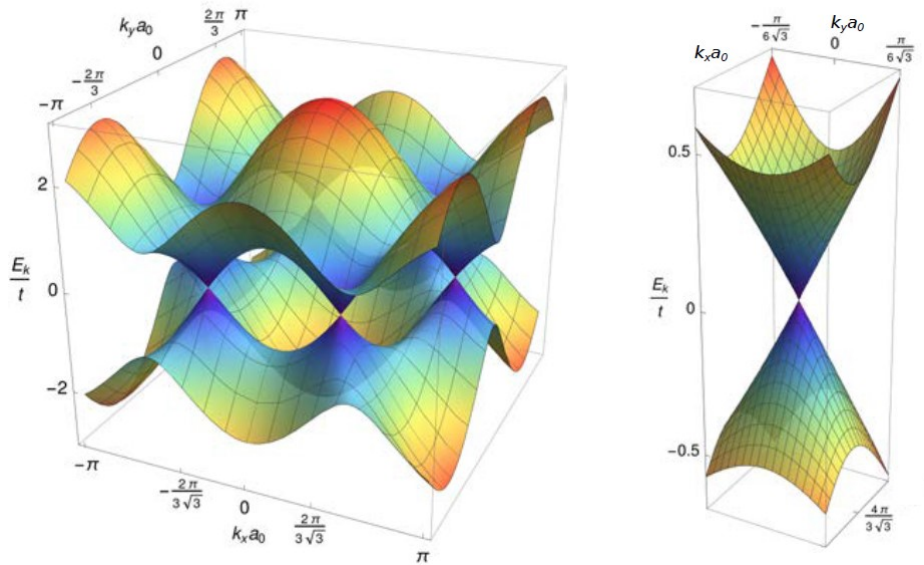

Figure 2.12: Electronic band structure of graphene. Right: zoomed region near the Dirac point of a reciprocal space

2.3.2. OPTICAL PROPERTIES

An interaction of graphene layer with light is typically described by complex optical conductivity function, which is linked to the dielectric function. Optical conductivity of graphene, is viewed as a sum of contributions from inter-band and intra-band transitions as

$$\sigma_g(\omega) = \sigma_{intra}(\omega) + \sigma_{inter}(\omega), \tag{2.39}$$

where the terms on a right side can be expressed, according to Kubo's formulation [70], as

$$\sigma_{intra}(\omega) = \frac{\sigma_0}{\pi} \frac{4}{\hbar\gamma - i\hbar\omega} \left[E_f + 2k_B T \ln 1 + e^{E_f/k_B T} \right], \tag{2.40}$$

$$\sigma_{inter}(\omega) = \sigma_0 \left[G(\omega/2) - \frac{4(\omega + i\gamma)}{i\pi\hbar} \int_0^{+\infty} \frac{G(E) - G(\hbar\omega/2)}{(\hbar\omega)^2 - 4E^2} dE \right], \tag{2.41}$$

where E_f is Fermi energy, being the energy level of the highest band filled, $\sigma_0 = \frac{\pi e^2}{2h}$ is graphene's characteristic conductivity, h and $\hbar$ Plank's constant and it's reduced version respectively, and

$$G(x) = \frac{\sinh \frac{x}{k_B T}}{\cosh \frac{x}{k_B T} + \cosh \frac{x}{k_B T}}, \tag{2.42}$$

where k_B is Boltzmann constant.

As in the case of metals, described in the first section, plasmonic phenomena is related to energy transitions within the conduction band, which, in the case of graphene, dominate at THz to mid-IR spectral region, where the inter-band contribution is negligible. The borderline between inter-band and intra-band transition lies around $2E_f$ region, where the real part of conductivity approaches σ_0 as depicted in the figure 2.13. It is easy to notice the resemblance of the equation 2.40 to a dielectric function based on the Drude-model, containing the relaxation frequency γ i.e. an average damping rate caused by lattice interactions, impurities and defects. *Ab-initio* computation of this parameter is a difficult task. Therefore, within the Drude approximation, it is possible to define relaxation frequency as $\gamma = \tau - 1 = \frac{ev_f}{\mu E_F}$, where μ is experimentally measurable carrier mobility, which, for exfoliated graphene, is in the order of 10000 $cm^2/(Vs)$ and for chemically deposited is about 7000 $cm^2/(Vs)$ [27], [71].
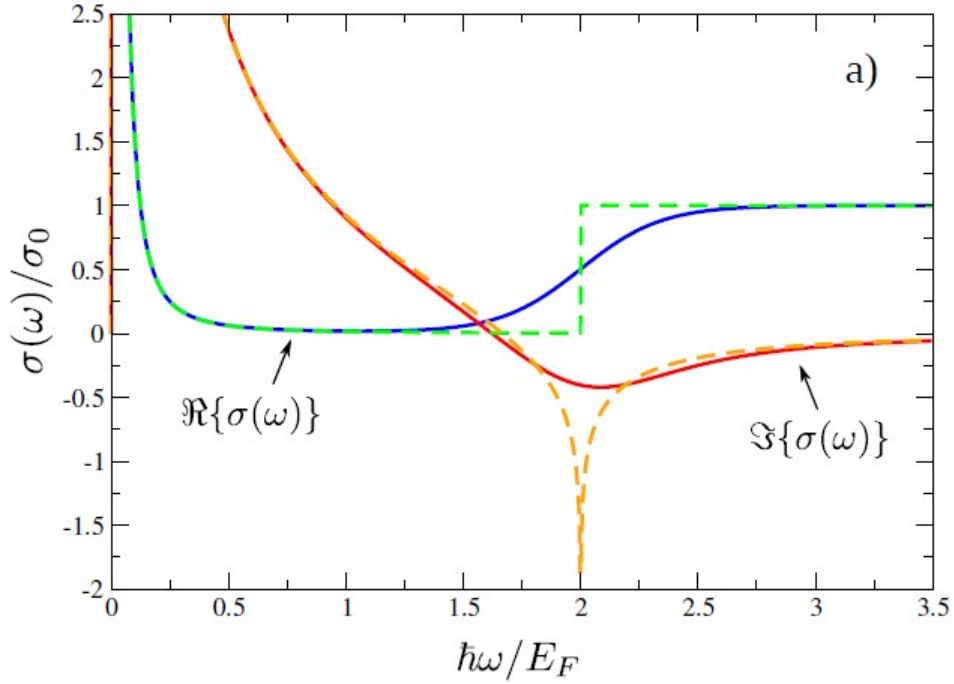
Figure 2.13: Real (blue) and Imaginary (red) part of surface conductivity function based on Kubo model- equations 2.40, 2.41. Solid lines represent conductivity at 300K, dashed curve - at 0K. [69]

2.3.3. GRAPHENE FABRICATION AND MODIFICATION

Due to semi-experimental nature of this work, it is necessary to touch upon the practical issues related to the graphene fabrication and its subsequent modification. It has been almost two decades since the successful isolation of graphene was achieved, but even now the fabrication process is still a "bottleneck" for further development of graphene electronic applications and large-scale production.

A plethora of methods have been developed to reliably produce monolayer graphene. The initial "breakthrough" technique was introduced by Geim and Novoselov [21] in 2004, and, essentially, it is a mechanical exfoliation of graphite using an adhesive tape. Despite the simplicity, this technique allowed researchers to reliably produce sufficiently large flakes of graphene. Top-down exfoliation of graphite has been further developed into several similar methods such as chemical, electrochemical and thermal exfoliation, sonication, ball-milling exfoliation and even cutting ("unzipping") of carbon nanotubes. These methods use Higly Oriented Pyrolitic Graphite (HOPG) as a precursor.

Bottom-up approach is by far more popular and it involves depositing layers of graphene

from liquid [72], gaseous [73] and solid chemical precursors [74]. Similar quality of graphene is produced by these methods and the choice is based on the availability of precursors and deposition systems as well as on the hazards associated with the procedure.

None of the above-mentioned approaches are able to synthesize graphene directly onto a silicon wafer. Currently, the deposition can only be done directly onto an oriented metal substrate, such as copper or nickel. Both exfoliation and deposition method require a transfer procedure. Typically a multistage transferring procedure is required to relocate graphene sheet to the final substrate. For chemically deposited graphene a general transfer procedure consists of covering the sheet with a protective layer, etching away the substrate by dry or wet chemical methods, subsequent transfer to the target substrate and removal of protective layer. It is obvious that such procedure will inevitably introduce contamination, decreasing the final purity of graphene layer [75].

The last step in the fabrication of graphene based devices is modification and patterning. Modification of local properties and surface chemistry of graphene includes selective oxidation and [76] or laser irradiation [77], and patterning mostly relies on the photolithography or e-beam techniques. Recently, however, with the introduction of commercial ion-beam microscopy, new method became available and it has proven to be a reliable method with superior resolution compared to conventional photolithography and with higher throughput (in case of graphene patterning), compared to E-beam lithography [78]. This method is exclusively used in this work and therefore deserves the additional description. Direct-write ion milling method is based on the irradiation of a material with focused beam of energetic (10-30 keV) helium or neon ions. They carry a high probability to sputter away atoms from the surface. It has been demonstrated [79], that this method is highly suitable for the milling of two-dimensional materials. Figure 2.14 shows two examples of patterning graphene and MoS_2 with helium ions. Notably, ion milling produces extremely well defined patterns with low edge defect, at least for freestanding layers. In the case of layers resting on top of a substrate, the milling process will be affected by substrate sputtering and increased backscattering probability for incoming ions. Nevertheless, the alternatives require a deposition of photosensitive polymers, introducing a persisting contamination to the patterned material, which in the case of atomically thin graphene may substantially compromise its electronic properties.
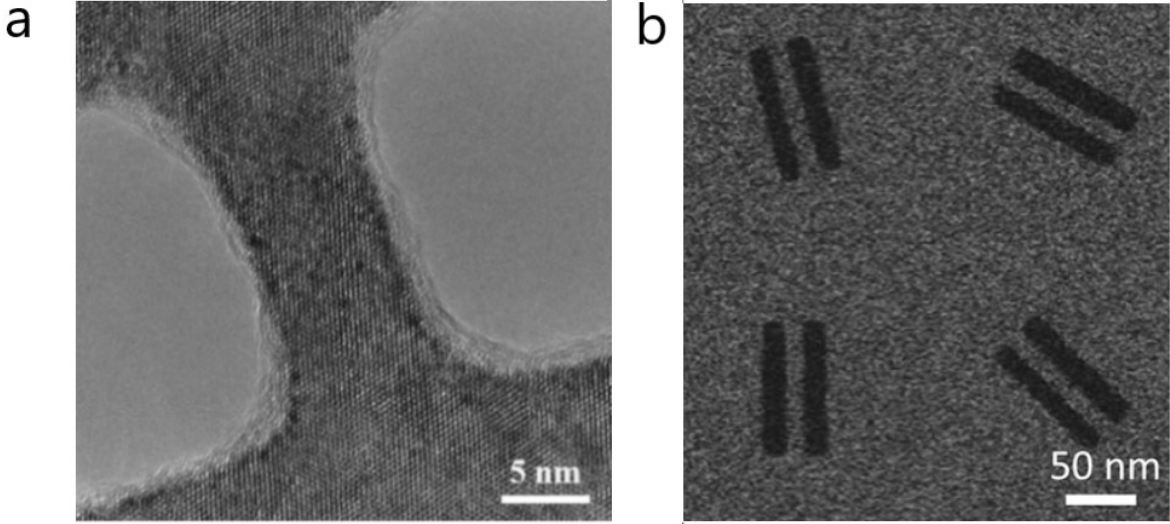
Figure 2.14: a) Transmission electron microscope image of freestanding MoS$_2$ ribbon formed between two areas milled by focused helium beam b) Scanning electron microscope image of freestanding graphene ribbons, each produced by milling away two rectangular areas [79]

2.3.4. GRAPHENE PLASMONICS

This work focuses on studying the plasmonic phenomena in graphene, more specifically - localized modes occurring in graphene nanostructures. This section provides a general description of both fundamental plasmonic regimes and summarizes current stage of computational and experimental researches. Using the approach demonstrated in the section 2.1.2 of the present work, the plasmonic dispersion relation for graphene layer resting between two dielectric media (ϵ_j) can be expressed as

$$\frac{\epsilon_1}{\kappa_1(q,\omega)} + \frac{\epsilon_2}{\kappa_2(q,\omega)} + i\frac{\sigma(\omega)}{\omega\epsilon_0} = 0, \tag{2.43}$$

where $\kappa_j = q^2 - \omega^2\epsilon_j/c^2$ is the decay constant in z-direction and $\sigma(\omega)$ is the complex optical conductivity of graphene described by the intra-band conductivity model in the equation 2.40 [69]. This equation is not solvable analytically, however, it can be seen that it has the real solution only when $Im\{\sigma(\omega)\} > 0$ and $Re\{\sigma(\omega)\} = 0$ which corresponds to the region of negligible damping $\gamma = 0$. However, in the real case scenario, when damping is present, the vector q will have a complex component that is related to the attenuation of surface plasmons. The equation 2.42 can be simplified, assuming that dielectric constants of surrounding media are equal, in the zero-damping region the dispersion relation of SPP can

be expressed as

$$\hbar\omega_{SSP} \approx \sqrt{\frac{2\alpha}{\epsilon}E_f\hbar q},\tag{2.44}$$

where $\alpha = \frac{e^2}{4\pi\epsilon_0\hbar c}$ is the fine-structure constant [69]. This relation shows an important feature of graphene plasmonic modes, which is a not only a spatial dependence on q vector, but also on the Fermi-level of graphene. The Fermi energy level is intimately connected with carrier concentration, $\propto n^{1/4}$, and can be readily modified by electrostatic or chemical doping. Practically, the former means that the plasmonic resonance of graphene can be tuned after the fabrication. Figure 2.15 demonstrates the plot of dispersion relation 2.42. The dispersion curve is always on the right side of the light line for the zero-damping case. With scattering introduced, the dispersion curve intersects the light-line at a very low q, however, because of the damping itself, no sustained excitation are possible there. Hence, similarly to metal, graphene plasmons are not excitable directly by the incoming radiation. Therefore, the same phase-matching techniques mentioned in the section 2.1.2, such as prism, grating and near-field coupling are fully applicable for graphene.
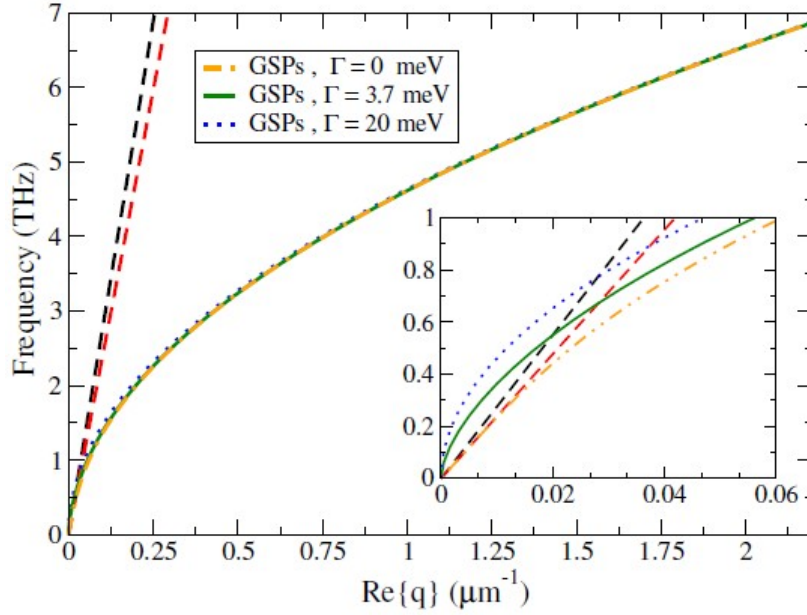

Figure 2.15: The dispersion of graphene surfce plasmons for different values of damping energy $\Gamma = \hbar\gamma$. [69]

Naturally, graphene can also support non-propagating plasmonic excitations (LSP) which occur in two-dimensional nanostructures. The simplest pattern, that has been extensively studied, is the array of nanoribbons, disks and nanorings arranged in a grid-like order. The example of numerically calculated dispersion of graphene nanoribbon are shown in the

figure 2.16. Unlike a dispersion in a continuous layer of graphene, plasmonic excitation in spatially confined structures branch into multiple curves each representing an normal mode. This behavoir is similar to the behavior of localized plasmon in nanoparticles being a dipolar oscillations of charge density. Higher modes are subjected to the "Landau damping" [28], effect associated with electron-hole transitions, and hence these modes are not visible in the experimentally obtained spectra, however experimental data well matches the prediction of the fundamental mode dispersion (figure 2.16) [27], [28], [35], [69], [80].
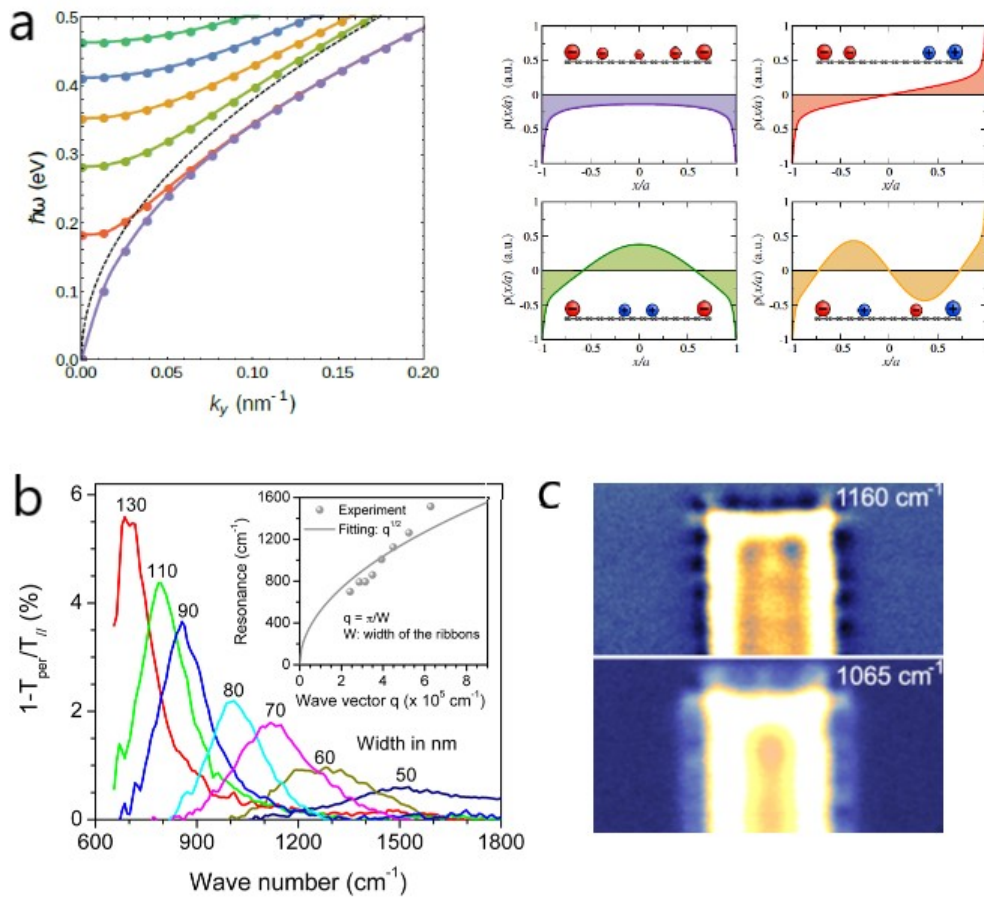

Figure 2.16: a) The dispersion curve of periodic array of graphene nanoribbons, $E_f = 0.5eV$ and charge density distribution of 4 lowest modes of a single ribbon [69]. b) Experimentally measured absorption of the array of graphene nanoribbons with varying width [28]. c) experimental visualization of the near-field intensity in a single graphene ribbon at different excitation frequencies. [81]

The unique spectral range of plasmonic excitation along with intrinsic tunability of optical response made graphene a highly promising material for sensing applications and

spectroscopy. For SERS, graphene demonstrated a substantial chemical enhancement of the 10^3 order [33], [34]. The topic of this work, however, concentrates on electromagnetic enhancement that is applicable for the infrared absorption spectroscopy. A number of convincing experimental results, focusing on graphene-based SEIRA, has been published [31]–[33], [82]. Spectra, presented in the figure 2.17 show distinctive fingerprints of particular molecular moieties and tunability over the wide range of frequencies. Identification of gas and solid phase analytes have been demonstrated. Reported areal concentration of sampled molecules is as low as 500 zeptomole/cm^2. Compared to other (metals and semiconductors) materials used in SEIRA applications, graphene demonstrated high spatial confinement of plasmons and, thus, a significantly smaller dimensions of plasmonic antennae. Notably, all experimental results were produced with the simplest periodic arrangement of nanoribbons which was chosen to simplify the fabrication of the chip. Arrangement of ribbons with one-dimensional periodicity is easier to incorporate into an electric circuits, need for gating purposes, by fabricating a simple metallic grid. Two-dimensional patterns,however, require a different approach for that matter. Ion gel, being a conductive liquid encapsulated inside polymer matrix [83], has been proposed as a possible solution for 2D nanodisk or similar patterns with separated plasmonic unit cells.
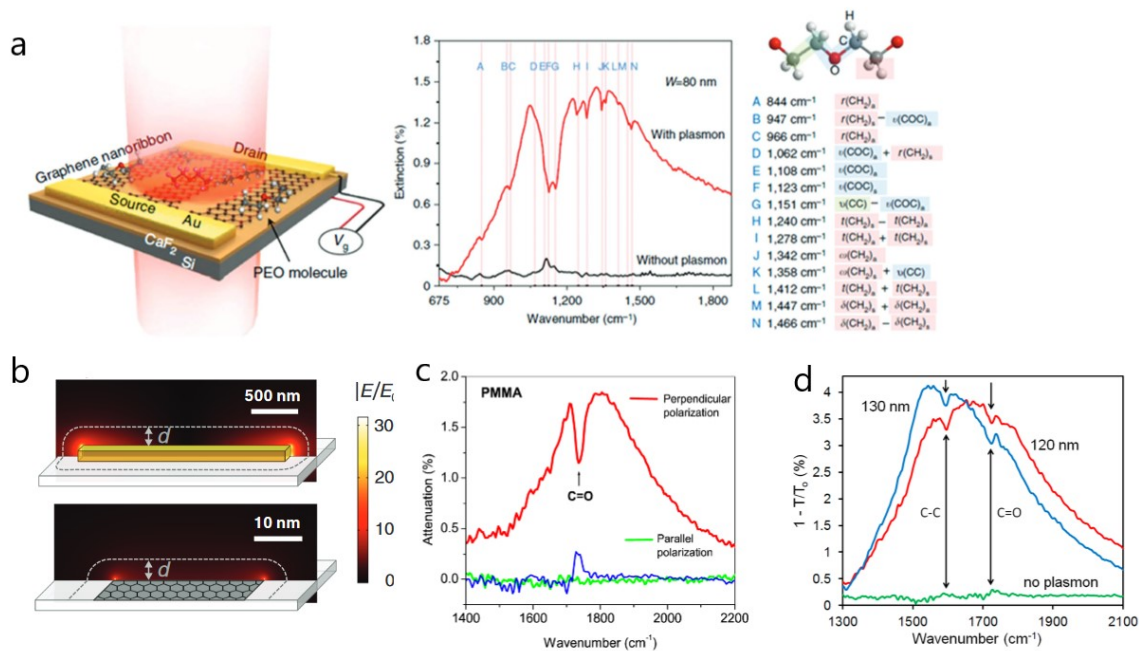
Figure 2.17: a) Conceptual representation of the SEIRA active surface composed of graphene nanoribbons and molecular fingerprint of PEO film measured with this device. b) Dimension comparison between metal and graphene plasmonic antennas operating at the same frequency. c) Attenuation spectrum of PMMA and d) PTCDA coated graphene plasmonic surface. [31]–[33], [82]

Based on its current stage, the further development of graphene as an active material for SEIRA, will largely rely on the advances in the fabrication of graphene nanostructures. The edge defects and contamination introduced during transfer deposition and patterning have a severe effect on the local electromagnetic enhancement and the lifetime of plasmonic excitations. Another apparent issue is providing the voltage for complex patterns where unit cells are not connected to each other. From the design perspective, computational research should focus on modelling nanoantennas to maximizing the areal concentration of plasmonic hotspots and the enhancement they provide.

This concludes theoretical section on graphene plasmonics. It was demonstrated how plasmonic characteristics of graphene arise from its structural and electronic properties. Using the framework developed for Drude-metal, dispersion relations of propagating and localized surface plasmons were derived. Distinctively, plasmons in graphene are characterized by tight confinement of light and electrostatically-tunable optical response. The last section demonstrated current results in graphene-based SEIRA development, highlighting some of the important research topics.

3. RESEARCH METHODS

3.1. COMPUTATIONAL DESIGN OF PLASMONIC ANTENNAE

Computational optimization of plasmonic geometries utilized Finite Difference Time Domain (FDTD) method implemented in commercially distributed software (Lumerical). This method is widely used to perform electromagnetic simulations for a variety of materials and complex geometries. FDTD approach solves Maxwell's equation in the time domain by simulating an evolution of electromagnetic field in a discredited simulation space. The spatial discretization is achieved by dividing the space into cubic cells, called an Yee-cell, demonstrated in the figure 3.1. Components of field vectors are assigned to edges and face-normal directions of each cell. The simulation starts by setting all fields to zero. Then the wave is "injected" at some position representing a source of radiation, which could be a plane wave, Gaussian beam, oscillating dipole, etc. Magnetic fields are calculated first followed by calculation of electric field components. Both fields are re-evaluated each iteration after a simulation time interval Δt. The simulation ends after a certain response threshold is reached and, usually, it is dictated by an estimated amount of energy left in the simulated region.

It is important to consider boundaries of a simulation space. For open-space geometries, ideally, fields must extend to infinity, which is not computationally possible. Therefore an artificial material, perfectly-matched-layer (PML), is added to boundaries of a simulation region to prevent any reflections from boundaries. For periodic structures, the algorithm supports corresponding boundary conditions, translating a simulated region along periodic directions. The data is recorded at specified regions of interest. Absorption and transmission data is recorded as an integral of power flow through a plane. This data can be used to extract spectral information and field distribution over the monitored plane.
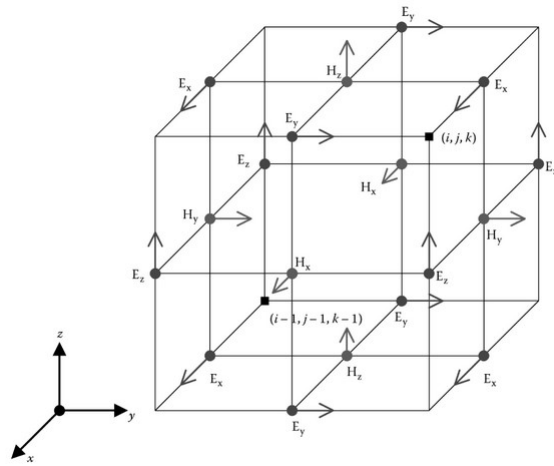
Figure 3.1: A discrete unit of space used in FDTD calculations [84]

Numerical approach always implies the existence of an error originating from a discrete nature of computers. Both space and time are treated incrementally with finite precision. Smaller step size usually produces more accurate results, but requires more computational resources and time. Thus, there is always an interplay between computational accuracy and available resources.

The biggest source of error in FDTD calculations comes from the spatial meshing. The size of the mesh defines an overall "resolution" of the simulation, and must be set to adequately resolve the objects of a simulation region. As a "rule of thumb", the maximum mesh size is set in respect to the lowest simulated wavelength, dimensions on an object and refractive index of medium. It should be noted however, that there is a fundamental limit of accuracy associated with finite precision of decimal numbers. Decreasing mesh size to extremely small values will introduce new source of error after a certain threshold. Rectangular geometry of Yee-cell is a source of an error itself, causing the "staircase" effect around curved geometries. Several meshing algorithms has been proposed to solve this issue [85], however this source of error should be considered for any curved geometry. Additional errors may arise from inadequately set dimensions or a duration of a simulation and a number of PML layers. In order to correctly set these parameters, an error estimation procedure must be conducted. In most of the cases, simulated problems are not solvable analytically and might not have an reference data. Hence, the estimation of an error is done by comparing numerical results within a single parameter "sweep". A relative $\Delta\sigma(i)$

and absolute $\Delta\sigma_N(i)$ errors of iteration, i, can be calculated as

$$\Delta\sigma(i) = \sqrt{\frac{\int(\sigma_i - \sigma_{i-1})^2 d\lambda}{\int(\sigma_i)^2 d\lambda}},$$

(3.1)

$$\Delta\sigma_N(i) = \sqrt{\frac{\int(\sigma_i - \sigma_N)^2 d\lambda}{\int(\sigma_i)^2 d\lambda}},$$

where σ_i and σ_{i-1} are spectral data of a current and a previous iteration respectively and σ_N is a reference spectrum.

The simulation region, used in this work, is shown in the figure 3.2. The simulation assumes graphene as a 2-dimensional material with Drude-based surface conductivity model expressed by the equation 2.40 with 2 adjustable parameters - Fermi energy level E_f that quantifies electrostatic doping, and damping energy $\Gamma = \hbar\gamma$, which are set to 0.5 eV and 1 meV respectively according to average values used in the literature [69]. Graphene is positioned on top of the SiO$_2$ substrate placed in parallel to x-y-plane. The refractive index data for silica is imported and fitted from the "Book of Optical constants" [86]. Electromagnetic plane wave is injected from the "source" at normal incidence into a negative z-direction. The wavelength range of the source is set to span 10-20 μm. Transmitted and reflected signals are registered by corresponding plane-monitors placed below the substrate and above the source. Additionally, a field profile is recorded in the graphene structure plane. Along z-axis, the simulation region was limited by perfectly matched layers. In x and y directions the boundaries are defined as periodic. Several types of meshes are used:

- coarse mesh in x,y z-directions spanning the whole simulation region
- fine mesh in z-direction resolving evanescent field around graphene layer
- fine gap mesh in x-y direction for resolving critical areas of structure
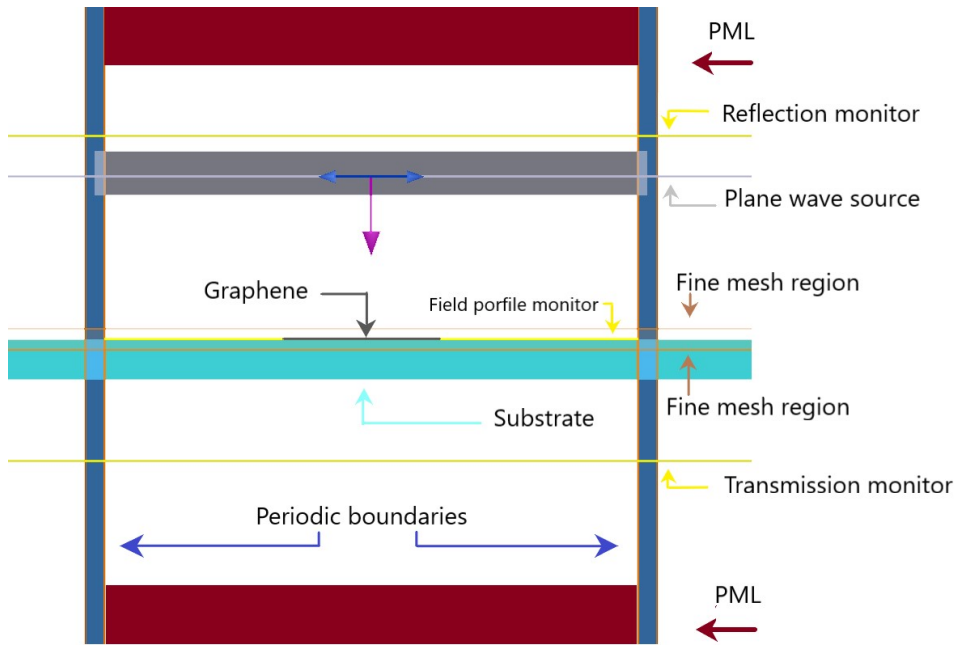- super-fine mesh in z-directions resolving graphene interface

Figure 3.2: The structure of the simulation setup for periodic graphene structures.

Parameters were optimized by calculating relative and absolute errors (eq. 3.1) in a series of convergence tests. These tests included variations of mesh sizes and spans, simulation region size, a number of PML layers and optimal duration of the simulations. Results of error tests are presented in the Appendix section. The largest source of error originated from z-resolution in the vicinity of graphene layer and gap mesh size. Final parameters were set to fit the experimental data presented in the figure 2.16. The size of the super-fine mesh cell was set to 2 nm, spanning 5 nm around the layer of graphene. The evanescent fields in z-directions were resolved by 7 nm mesh spanning 500 nm. Gap regions were resolved by the 5 nm fine mesh in x-y direction. This resolution was chosen on the basis of fabrication capability of e-beam and focused ion beam lithographies, which can reliably reproduce features >5 nm in size. Figure 3.3 shows the result of simulation benchmarking. Numerical spectra are sufficiently close to the published experimental data [28], deviating less than 5%.
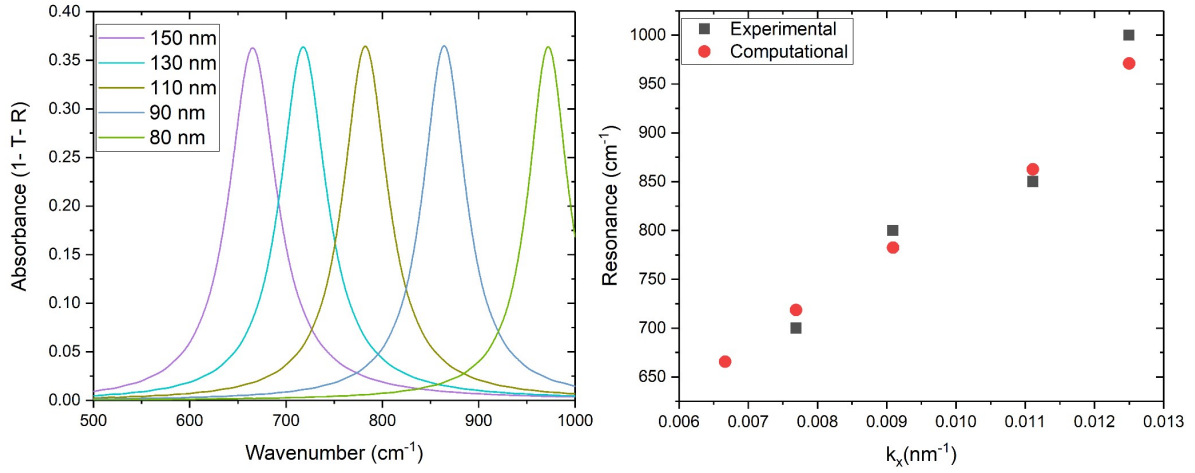
Figure 3.3: Left: Simulated spectrum of nanoribbons with varying width. Right: corresponding dispersion of simulated nanoribbons plotted against the experimental data provided by Avouris et al. [28]

The main goal of the computational work was to evaluate the set of graphene plasmonic antenna designs based on simple geometrical shapes, such as triangles, disks and rectangles. For each geometry, a variation of plasmonic response with the size of a structure was analysed by computing absorbance, defined as $A = 1 - T - R$, where T and R are transmission and reflection spectra. Resonant frequency shift that corresponded to the dimensional variation allowed calculating the plasmonic dispersion, k_x vs the resonant frequency. The wave vector representation is used to describe collective plasmonic excitation in periodic structure and it is defined as $k_x = 1/d_x$, where d_x is the length of structural dimension parallel to the electric field component of the incident plane wave. Furthermore, a response to polarization angle variation was computed for each nanostructure. Electric field profile was calculated by measuring power flow through the plane of graphene and performing the Fourier-transform operation to obtain a spectral distribution. The highest value of the electric field at each frequency was collected. Additionally, the field profile, over the area of an antenna, was sampled at each plasmonic peak frequency. The profile was used to compute the effective mode area, A_{eff}, of plasmonic excitation. The equation for effective mode area is expressed as

$$A_{eff} = \frac{(\int_A |F(x,y)|^2 dA)^2}{\int_A |F(x,y)|^4 dA},$$
(3.2)

where $F(x,y)$ is a profile distribution function of either magnetic or electric fields. The equation is similar to Landau-Lishitz approach, in which the mode area is calculated by taking a ratio of mode energy density per unit length and peak energy density [87]. The mode area along with the peak value of the electric field was used to evaluate the efficiency

37

of each pattern by quantifying the field enhancement and concentration of the field over the area of a plasmonic cell.
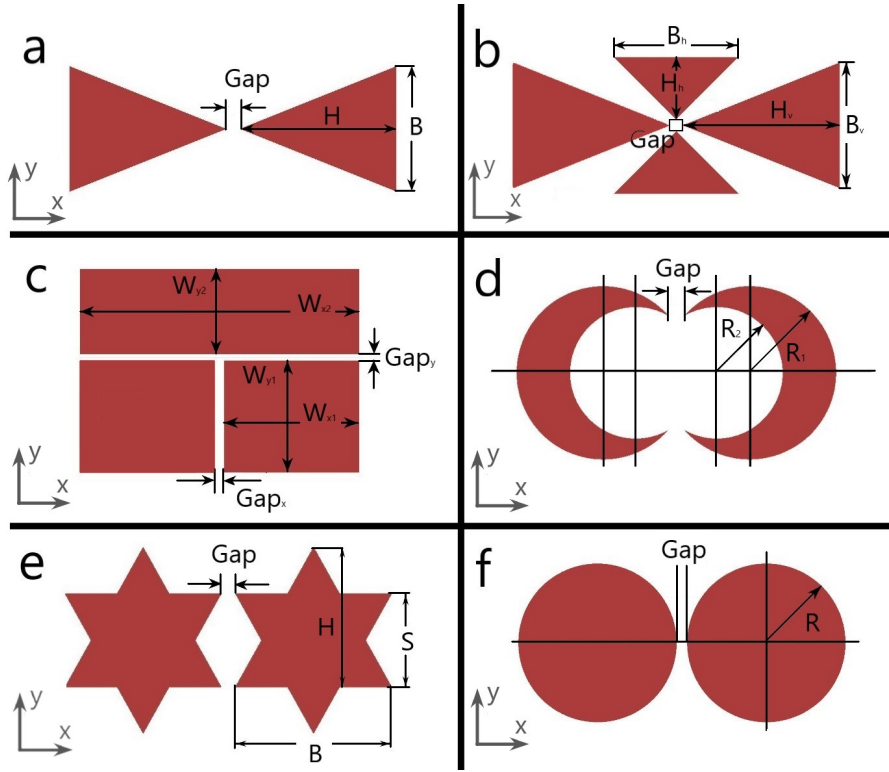

Figure 3.4: Proposed designs of graphene plasmonic antennae: a) bowtie, b) double bowtie c) rectangular tiles, d) crescent dimer, c) hexagram star dimer, e) disk dimer

Six antenna geometries (figure 3.4), based on three-dimensional plasmonic metallic nanostructures reported in literature, were proposed. A common theme in these geometries is the presence of a small spacing, gap, formed between extremities of neighbouring structures. This gap forms a "hot-spot" area of increased field magnitude. The surface density of hot-spots as well as the field enhancement within the hot-spot are directly related to the total enhancement of infrared absorption signal. Three structures are based on triangle-shape - bowtie and double-bowtie patterns, as well as hexagram-star which are composed of isosceles triangles defined by the height H and the base B. In hexagram geometry, triangles are shifted by the distance $S = 0.75H$ and the height, H equals the base, B. The tile geometry is based on rectangular ribbons with 2 different width along x axis - W_{1x} and $W_{2x} = 2W_{1x}$ and equal span in the y-direction W_y. Two other structures are based on a nanodisk shape - disk and crescent dimers. Disks are described by the radius R and crescent - by the radius R_1 and the radius of inner "cut-away" circle $R_2 = 0.75R_1$, shifted by the distance $\frac{1}{2}R_1$ in the x-direction. If not stated otherwise, all the numerical simulations, for

each dimer illustrated in the figure 3.4, were performed with the longitudinal plane-wave polarization by setting $\vec{E}$ parallel to the x-direction.

Electromagnetic response of all the designs was simulated within the range between 15 to 30 THz (corresponding to 500-1000 cm^{-1}). According to experimental data, graphene has a prominent plasmonic resonance in this range, with narrow peaks indicating a sufficiently low damping. This range is also hardly reachable by metal-based plasmonic structures.

3.2. EXPERIMENTAL METHODS AND MATERIALS

The aim of the the experimental work was to produce an active (voltage-tunable) plasmonic chip based on a nanostructured graphene. The first milestone was to replicate a device similar to the one described in the article published by Avouris et al. [28] and reproduce its results previously demonstrated in the the figure 2.16. Here, an alternative fabrication method for graphene patterning was chosen - instead of lithography, the focused ion beam sputtering was used.

3.2.1. FABRICATION OF GRAPHENE SUBSTRATE

Conceptual layout of the test chip is shown in the figure 3.5. The chip was designed to have several isolated grids with graphene layer transferred on top. Each grid unit has a separate contact pad for external voltage connection. The size of each grid unit is $500 \times 500 \ \mu m$, each unit consists of $100 \times 100 \ \mu m$ cells. A $50 \times 50 \ \mu m$ patterns were fabricated inside a selected cells. Conductive silver paste was applied directly to the silicon substrate to provide a capacitive connection to the grid. The edges were isolated with epoxy resin to prevent a short circuit between grids and the silicon. The chip was designed to fit a standard carrier socket which was embedded into a PCB board for external connection to a voltage source.
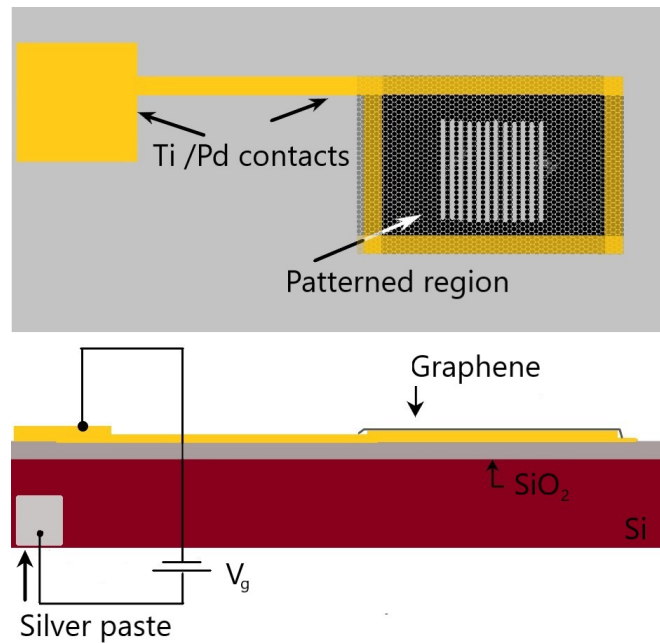
Figure 3.5: Conceptual design of the experimental plasmonic chip, top and side view. V_g depicts the gating connection.

The blank graphene chip used in this work was pre-fabricated with the assistance of M.Sc. Jyrki Manninen. The overall synthesis and transferring process consisted of the following stages:

1. deposition of copper substrate (600 nm) on top of (0001) sapphire

2. feeding diluted (5 sccm) methane/argon mixture was to an annealed (1060 C°) copper substrate

3. spin-coating graphene with ≈ 200 nm thick layer of PMMA

4. depositing 2 nm Ti/95 nm Pd grids onto a SiO_2 substrate with by e-beam lithography and evaporation

5. wet etching (Ammonium persulfate) was applied to remove copper substrate and release the graphene-PMMA stack

6. transferring graphene via water-HCl-water bath sequence to the silicon chip

7. removal of an old PMMA layer and application of a new one for large scale patterning (separation of graphene between grid-units)

8. final removal of PMMA, cleaning and annealing the sample at 300° simultaneously exposing to Ar/H_2 gas flow

The patterning of graphene was accomplished with helium ion microscope (HIM, model "ORION NanoFab") manufactured by Zeiss GmbH. A general introduction to the technique has been given in the section 2.3.3 and the schematic of HIM assembly is shown in the figure 3.6. The particular model used was equipped with helium/neon gas ion source. The ion beam is produced by the atomically sharp tungsten tip nested inside the cryo-column. Produced ions are accelerated towards the target with modifiable energy (typically 15-30 keV). The beam of ions is aligned and focused by the arrangement of electromagnetic lenses and apertures placed inside the column. The sample stage is equipped with electron detector used for imaging, and electron flood gun, used to compensate for the cumulative charge of ions. The microscope operates in the scanning regime. The beam is focused into sub-10 nm spot that is swept across the surface producing a detectable secondary electron emission at each point. Secondary electrons are used to reconstruct an image.
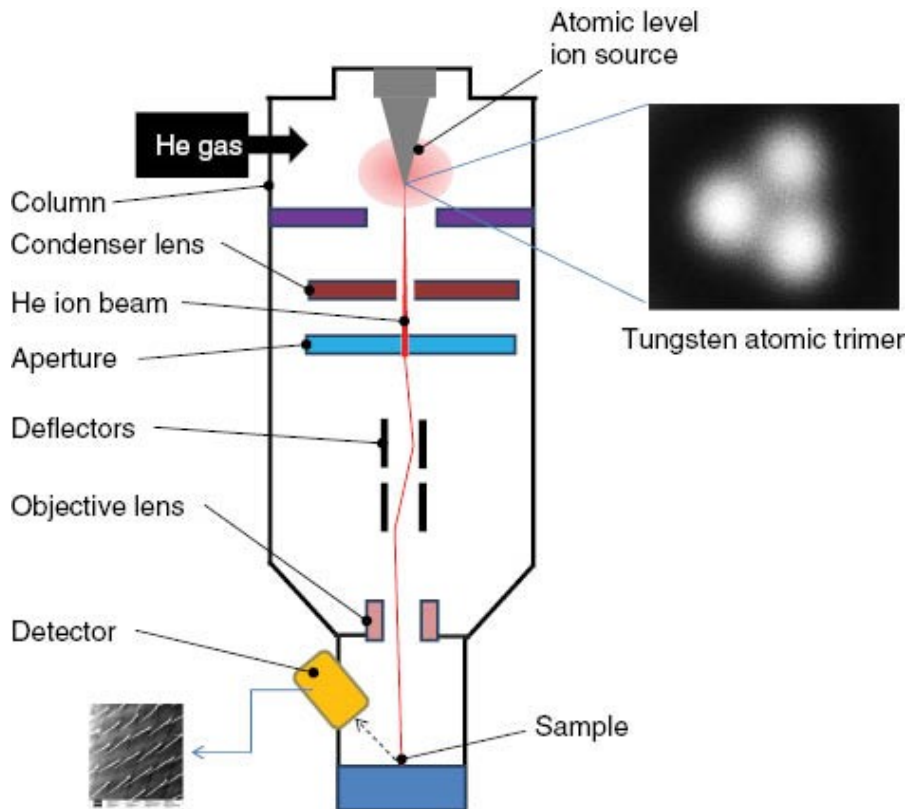

Figure 3.6: Schematic diagram of helium ion microscope assembly [88]

Accelerated ions can also be used to remove material layer by layer via the process called sputtering. It occurs when an atom of a substrate is being knocked by an incident particle

receiving a portion of its momentum. If the the momentum along substrate-normal direction overcomes binding energies the atom will be sputtered into the environment. The probability of this scenario is refereed to as a sputtering yield and is expressed in *atoms/ion*. This quantity can be directly used to calculate the irradiation dose, dwell time per spot, required to remove a monolayer of material by an ion beam with specified current (measured by the microscope).

There is a limited quantitative data published on sputtering yield for graphene by He and Ne ions [79], and all exciting publications describe sputtering of freestanding graphene. According to the elastic collision model that describes sputtering phenomena [89], an incident ion produces a cascade of recoil events in the material until it looses the energy. it is obvious, that substrate atoms and recoiled ions may also participate in the sputtering of a surface layer. Thus the value of sputtering yield in case of graphene resting on a substrate is expected to be greater than for suspended case.

Therefore, the first step of experimental work was to define sputtering parameters, ion type, energy and irradiation time, for the case of graphene placed on top of the silicon dioxide. In order to define the approximate value of irradiation dose, a series of Monte Carlo type simulations were conducted. The algorithm, based on the aforementioned model of inelastic scattering [89], is implemented in the free-distributed SRIM/TRIM software code. Every material is approximated as uniform media with specified density. The software simulates a random collision event, samples the outcome and updates the result statistics. The approximate representation of materials in the software does not account for numerous phenomena, such as the lattice tunneling, charge accumulation and, mainly, the transformation of target area under continuous ion beam irradiation. Thus, computed results are highly uncertain. However, they are a good estimated starting point for further experimental trials.

Graphene layer was simulated as a single layer of carbon atoms with density of 2.26 g/cm^3 (graphite), lattice energy of 5 eV [90], binding energy of 7.46 eV [91] and displacement energy of 27 eV [92]. Theses parameters quantify the lattice, inter-atomic bonding and the energy required to create Frenkel defect respectively. Parameters for the substrate were taken from the material database provided in the software. Each simulation contained 10^5 events. More details on patterning can be found in previous research project report [93].

3.2.3. SAMPLE CHARACTERIZATION

The sample was characterized using the atomic force microscopy, model "Dimension Icon" manufactured by Bruker, and FTIR microscope setup consisting of "Nicolet is50" IR-bench and "IR-Plan Advantage" optical microscope system.

Atomic force microscopy was a primary tool used to characterize the profile of the patterned structures. Its principle of operation is based on the measurement of height profile by a nanoprobe consisting of cantilever with atomically sharp tip, and piezo-scanner used for a high-precision positioning of the probe. The schematic diagram of generic AFM setup is shown in the figure 3.7. The tip scans along the surface of the sample in the x-y-direction, while the laser is used to register any deviation in z-position of the probe. The laser-beam is aimed at the edge of the cantilever and is reflected into a position-sensitive photo-detector. The signal of the photo-detector is recorded as the height profile information and simultaneously used to re-adjust the position of the probe through the feedback loop to maintain constant distance from the substrate. Recorded data is used to reconstruct an image based on the height profile of the sample.
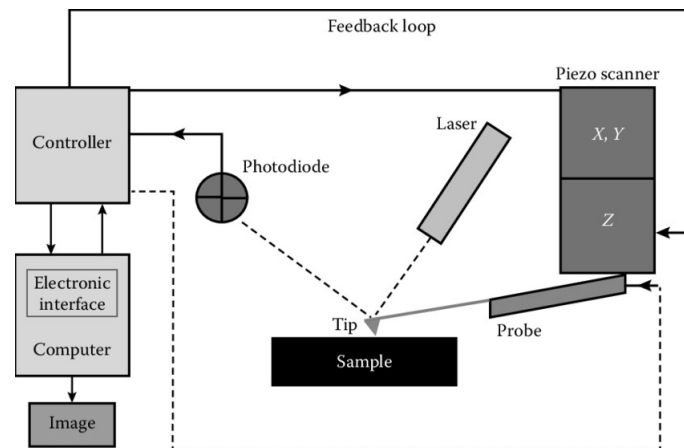

Figure 3.7: Schematic diagram of atomic force microscope set-up [94]

A typical AFM is able to operate in three distinct regimes - contact, non-contact, and tapping modes. As names suggest, the main difference between these modes is in the proximity of the probe to the sample surface. In the contact mode the cantilever is positioned so close to the surface that the tip starts experiencing a strong repulsive force. In the non-contact mode the tip is positioned further away from the surface and cantilever is oscillating with its natural frequency. In the lowest points, the tip may experience attractive force that causes deviation in the amplitude and phase of the oscillation. Tapping mode is an intermediate regime, in which the tip is positioned far enough to oscillate freely, however

at the lowest point of amplitude the tip comes into contact with the surface. The microscope used in this work is also able to operate in "peak-force" tapping mode regime, which allows setting the maximum tapping force. This method is extremely useful for imaging e.g. freestanding nanoparticles, graphene or deformable soft surfaces. For graphene, the peak force value of 0.1 nN was found to be suitable.

FTIR microscopy is based on the standard Fourier Transform Infrared absorption set-up connected to a microscope equipped with IR objective. The schematics of the setup is illustrated in the figure 3.8. FTIR system generates a continuous-wavelength signal which is modulated when passing through a Michelson interferometer. The interferometer consists of beam splitter and two mirrors, one of which is movable. The beam splitter divides the signal into two beams which are reflected back from mirrors and recombined. Changing position of the movable mirror causes an interference to occur, producing a modulated signal. The sample is irradiated by the modulated infrared beam and the reflected or transmitted infrared signal is then registered by the mercury cadmium telluride (MCT) detector cooled with liquid nitrogen. At the final step, the recorded signal is converted into frequency domain spectrum by Fourier transform. FTIR system can be incorporated with an infrared microscope to measure samples in reflection or transmission modes with higher resolution. The actual set-up operated in the range from 4000 to 650 cm^{-1} with spot size of 2 μm. The microscope was used in reflection mode to obtain the signal. Transmission mode measurement is preferable for graphene, however the design of the chip carrier prevented transmission of a signal through the sample.
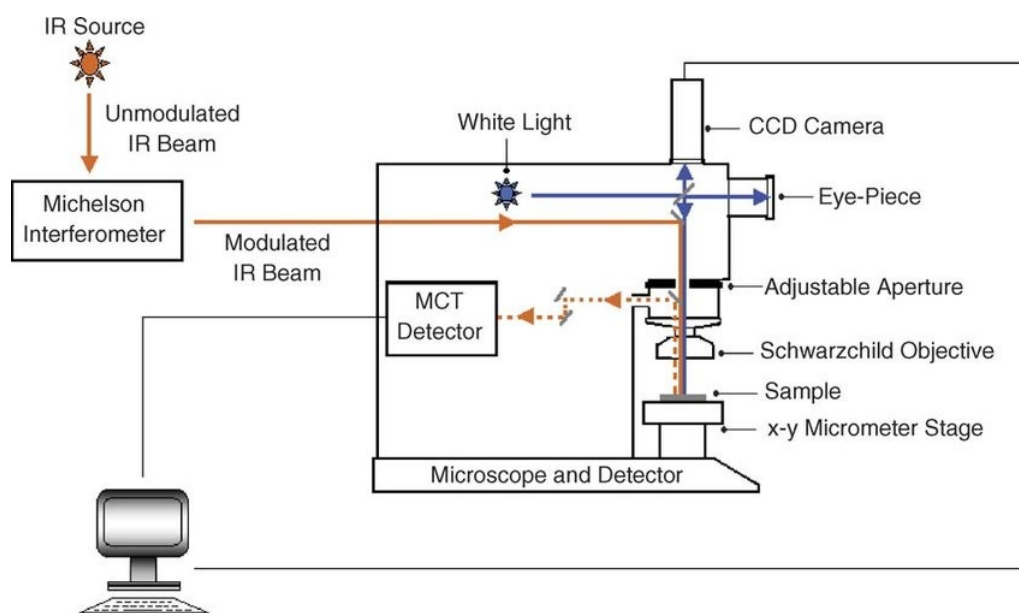

Figure 3.8: Schematic diagram of FTIR micrscope set-up [95]

4. Results and Discussion

4.1. Computational results

4.1.1. Dispersion relations

FDTD studies were performed for six 2-dimensional graphene antenna geometries. For each structure, the effect of primary dimension (parallel to $\vec{E}$ component of the incident plane wave) variation was computed. The gap between geometries was kept 10 nm, while the size of each structure changed. Dispersion relations for each geometry were calculated by performing a polynomial fit of the simulated data. The results are presented in the figure 4.1. According to the data, bowtie, double-bowtie and crescent geometries exhibit the greatest confinement factor as their dispersion curves are shifted towards a larger wave vectors compared to rectangular tiles (closely-spaced ribbons), disks and hexagram star. This translates into a significant size difference between different antennae operating at the same frequency. Subsequently, the areal density of plasmonic unit cells is affected. As an example from computed results, at 20 THz frequency, a single disk must have a diameter of ≈ 200 nm while the height of the active triangle in a double-bowtie antenna is ≈ 111 nm. This translates into $\approx 88 \cdot 10^3$ nm^2 area occupied by the disk dimer versus $\approx 29 \cdot 10^3$ nm^2 occupied by bowtie dimer unit cell. This is a rather significant difference - double-bowtie occupies ≈ 3 times smaller area. Assuming one hot-spot area per unit cell - the areal density of active zones also triples. It is straightforwardly seen from the fitting, that the dispersion of both bowtie geometries exhibit a saturating behavior, whereas the dispersion relations of other geometries are linear in the chosen frequency range. The size variation of triangle shapes in both bowtie arrangements seem to produce diminishing effect on the resonant frequency. It indicates that bowtie arrangements are not suitable for frequencies above 25 THz as the dimensions of each triangle will quickly approach the resolution limits of common fabrication methods.
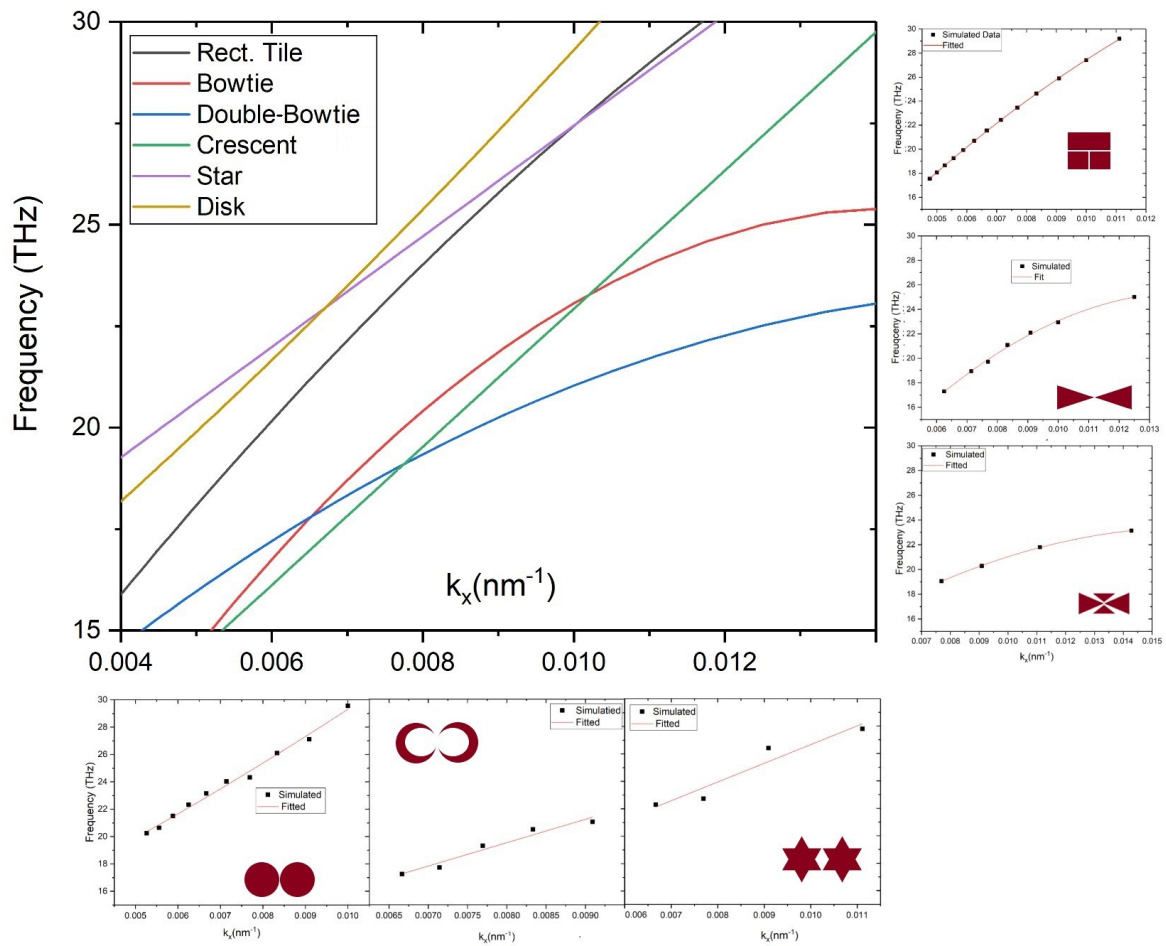
Figure 4.1: Dispersion relation curves of simulated graphene nanostructures based on numerical data fitting.

According to the formulation of the Purcell enhancement factor, equation (2.24), the figure of merit for an optical resonator efficiency, is the local field enhancement $\frac{E_{loc}}{E_0}$, which correlates with the geometry of an antenna and the dimensions of the formed between two plasmonic structures. In order to quantify this parameter, a series of simulation with varying gap between two adjacent nanostructures has been conducted. The sizes of each structures were kept constant, while the gap between them, as well as the distance to periodic boundary, were reduced. The results are presented in the figure 4.2.

Computed field profile distributions demonstrate substantial variation in the local enhancement between studied patterns. Bowtie and double-bowtie arrangements demonstrate the highest enhancement values of $2.5 \cdot 10^5$ and $1.6 \cdot 10^5$ respectively, while crescent shape demonstrates an order of magnitude lower enhancement at the same gap length. The rest of the structures exhibit similar enhancement factor of $\approx 5 \cdot 10^4$. Decreasing the separation distance also causes plasmonic resonance to red-shift. A drastic leap in the magnitude of the electric field, occurring when the gap reduces to 10 nm, indicates the near-field coupling regime. The scattering into far-field is suppressed, and the most of the plasmonic energy is concentrated inside the gap. It is especially visible in the case of double-bowtie spectra. Parasitic resonance peaks, caused by coupling between horizontal and vertical bowtie groups, disappear when the near-field coupling takes place.

Field distributions, demonstrated in the figure 4.3, show locations of the enhancement spots for each geometry. As expected, the largest magnitudes of the electric field at resonant frequency, are localized around sharp geometric features. In the near-field regime. the enhancement region is highly concentrated at the 10 nm gap formed between geometries. The energy of a plasmonic excitation concentrated in the gap contributing to the observed leap of the field magnitude at the excitation frequency.
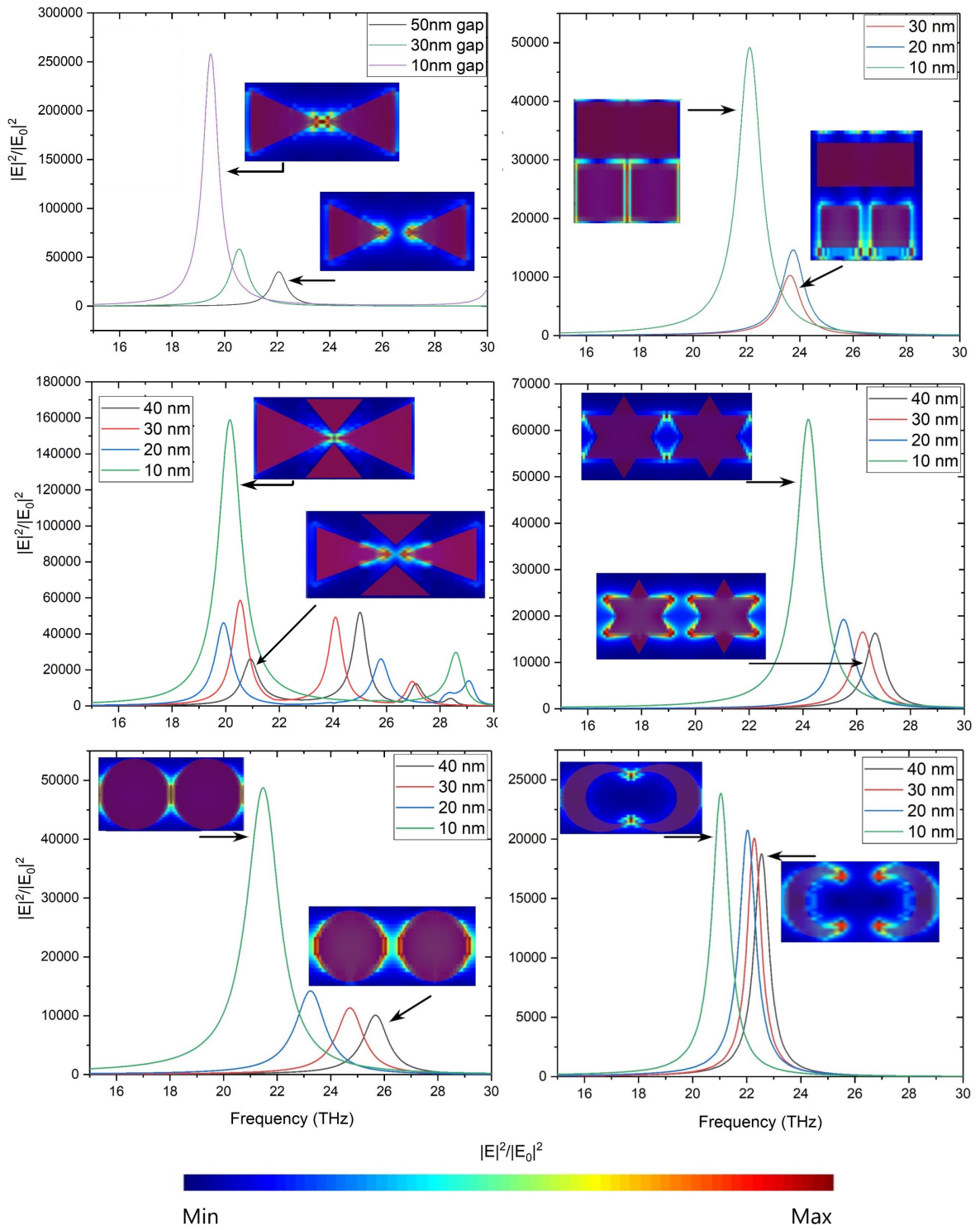
Figure 4.2: The effect of dielectric gap variation on local filed enhancement. Left column: bowtie, double-bowtie, disk dimer. Right column: rectangular tile, star, crescent. Insets represent near-field profile map at the resonant frequency.
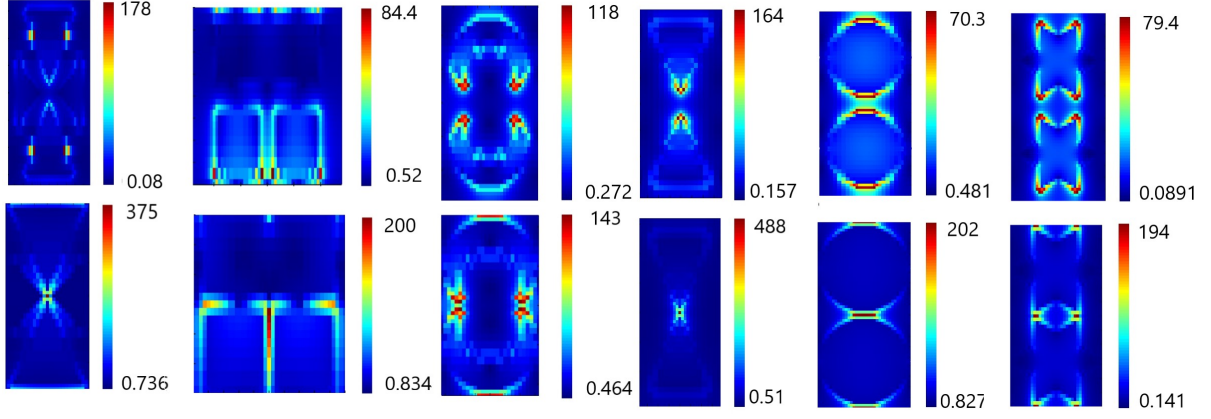
Figure 4.3: Electric field, $|E|/|E_0|$, distribution at excitation frequency for far-field (top row) and near-field (bottom) coupled dimers, corresponding to the gap variation shown in the figure 4.2. From left to right: double-bowtie, rect. tiles, crescent, bowtie, disk, hexagram

4.1.3. MODE AREA

The amplitude of the electric field at resonance is not the only parameter contributing to the efficiency of enhancing surface. The signal enhancement of SEIRA is also determined by a number of absorbing species affected by a resonant structure. Thus, it is important to consider the spatial distribution of the field in a unit cell. Since graphene is a two-dimensional material, the areal distribution of the field in the plane of resonant structure is considered. The effective area was calculated using the equation (3.2). The electromagnetic field profile was sampled at each frequency and integrated over the area of a structure cell. The resulted normalized effective area functions for each geometry are represented in the figure 4.4. In the similar manner with previous, the gap varied while the sizes of structures were kept constant.

The variation of mode area with the gap have shown different trends for studied geometries. In the case of disks, crescent and bowtie dimers, the mode area remained at the same level during the transition form far-field to near-filed coupling regimes. This behavior contradicts the observation of the field distribution in the figure 4.3, where two hot spots in the far-field regimes merge into a single spot. The reason for the observed dynamics is that the equation (3.2) takes into account the whole area of the plasmonic unit cell. Not only the hot-spot, but also the electric filed magnitude of its surroundings is taken into account. So the mode area calculation also accounts for the minimum values of the electrics field. This explains a rather unexpected growth of modal area in the double-bowtie arrangement,

49

the minimum electric field magnitude grow almost ten-fold, while the maximum enhancement value only triples.

In the near-field coupling case, all the structures, except disks and bowtie dimers, demonstrate same relative modal area, of about 85% of the cell structure. Disks exhibit the largest mode area of plasmonic excitation, approximately 92.5% , while the bowtie show the strongest confinement of the field, reflected in the smallest mode area, $\approx 80\%$ compared to the rest of the geometries. Considering its the high enhancement of the electric field, disk dimer utilizes the cell area more efficiently compared to other geometries. On the other hand bowtie provides the largest hot-spot enhancement, which may be preferable in the case an analyte species can be selectively absorbed inside the hot-spot zone.
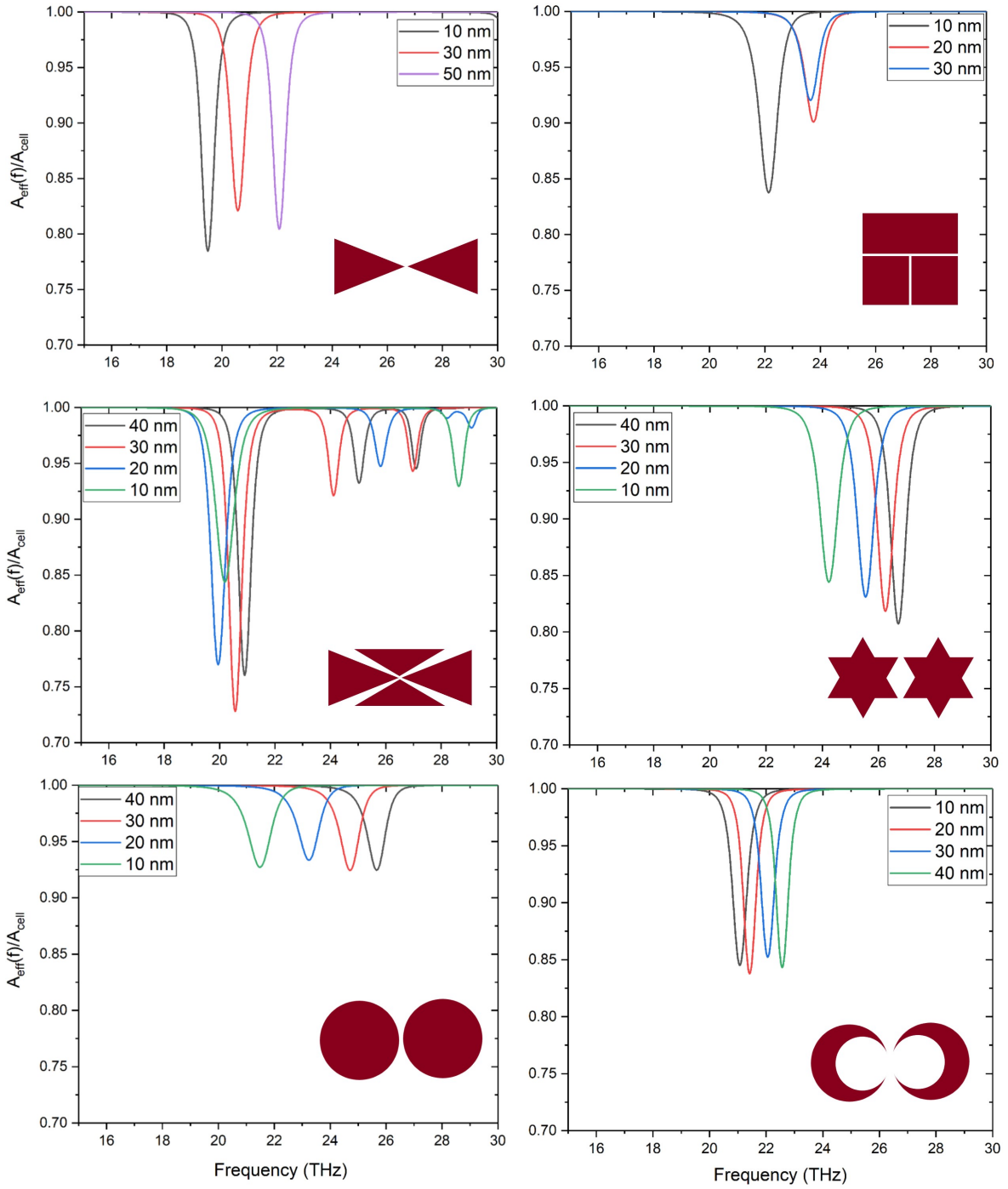
Figure 4.4: The mode area of plasmonic excitation calculated using the equation (3.2). Each curve corresponds to variation of gap between structures and neighbour dimers

One of the reason to investigate structures with two-dimensional periodicity is the ability to switch between resonant modes by changing polarization angle of the incident light. Figure 4.5 demonstrates how each structure respond to the change of polarization angle. It can be seen that disk and crescent dimers exhibit only single resonant mode, while star and both bowtie geometries feature 2 plasmonic modes available at perpendicular polarization angles. The rectangular pattern demonstrates 3 distinct resonant modes corresponding to different widths of upper and lower ribbons and their span in the y-direction. Compared to the basic one-dimensional arrangement of ribbons, rectangular tile structure offers a greater frequency reach, advantageous for spectroscopic applications.
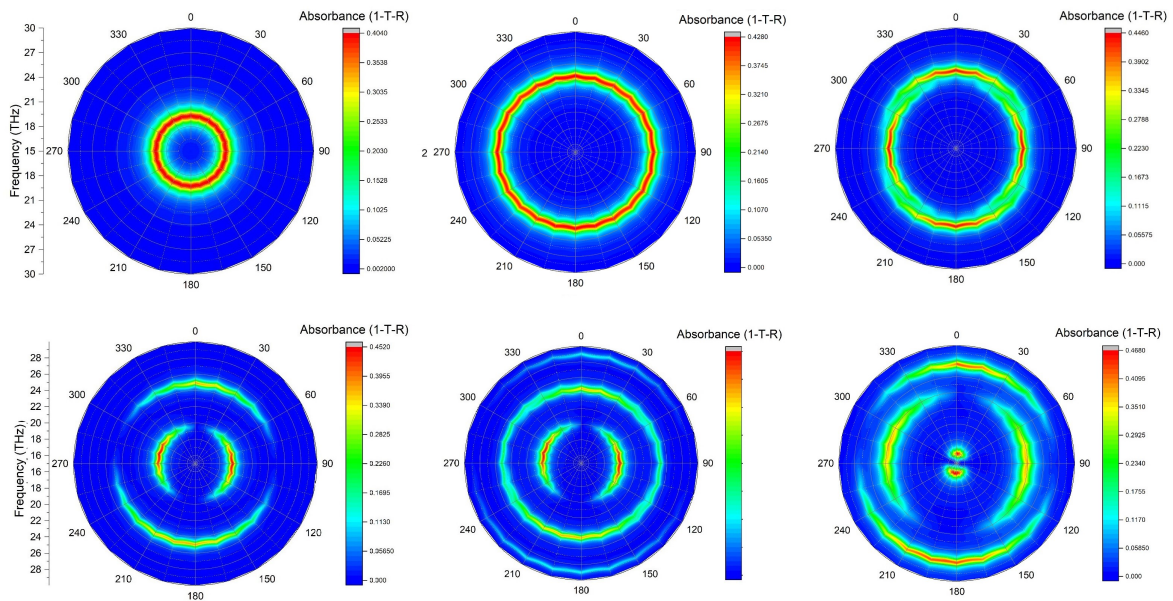

Figure 4.5: The effect of polarization angle on absorbance spectra of studied geometries. Left to right: top row - disk, crescent, star; bottom row - bowtie, double-bowtie, rectangular tile

The last set of numerical simulations were conducted to observe the effect of graphene optical conductivity variation. According to the Kubo's formula, equation (2.40), optical conductivity of graphene is primarily affected by the Fermi energy level, E_f, and electron scattering energy, Γ. Subsequently these parameters affect plasmonic properties of graphene. The Fermi level is altered via electrostatic gating or chemical doping, and the scattering parameter is related to carrier mobility and the overall concentration of defects. The ability to modify the Fermi level offer a real-time tunability of the plasmonic response as shown in the figure 4.6. By varying the level of electrostatic doping, it is possible to cover a broad spectral range with a fixed geometry. The variation of Fermi level from 0.2 eV to experimentally reported maximum of 0.8 eV [96] was computed. Such shift is sufficient to reach virtually any frequency in the chosen spectral range. The field enhancement follows the trend, remaining at the the same magnitude over the whole range o frequencies. The apparent contraction of the mode area merely corresponds to the reduction of the wavelength. Scattering rate variation has been tested for the range of 1 meV, corresponding to an ideal graphene, to 7 meV, representing experimentally observed scattering of high a quality CVD graphene [97]. The effect of increasing scattering rate is striking and confirms the issue of using graphene as a high-enhancement-factor plasmonic material. The values of the field enhancement at increased scattering energies are dramatically lower than in the case of "ideal" graphene. The expansion of the mode area indicates a lower field magnitude of a "hot-spot" compared to its surroundings.
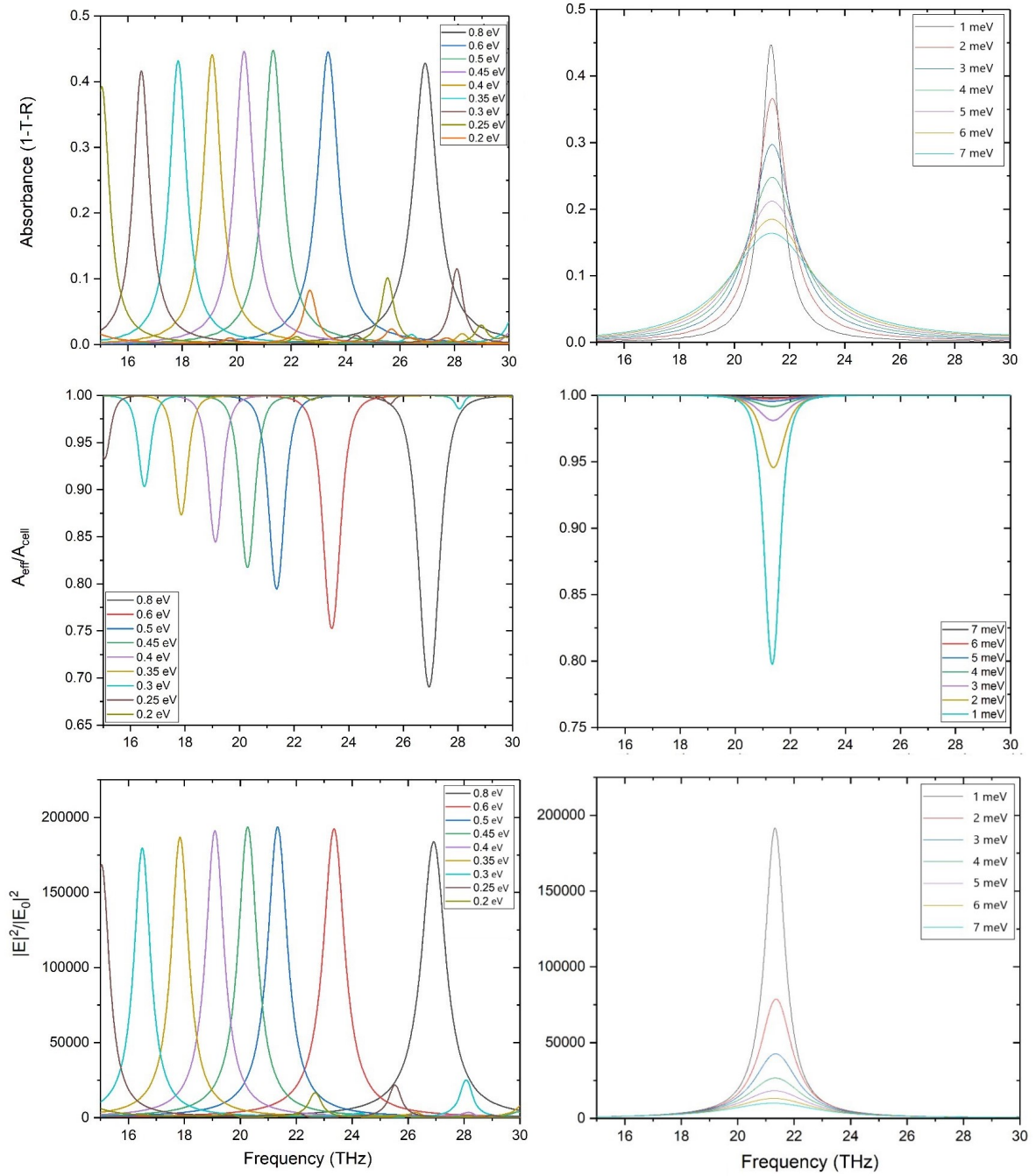
Figure 4.6: The effect of Fermi level (left column) and damping energy $\Gamma = \hbar\gamma$ right column) variation on the absorbance, mode area and field enhancement. Computations are performed for the bowtie geometry with

54

4.1.6. Conclusions of computational modeling

This concludes the computational section of the thesis. As it was demonstrated, graphene has an excellent potential to be used as active material in SEIRA. High confinement factor of graphene allows considerable reduction of the size of two plasmonic antenna compared to metal-based structures. The field enhancement values reach the same order of magnitude as in metallic nanostructures [82]. It was also demonstrated that two-dimensional geometry of proposed patterns enables multiplicity of available resonant modes, accessible via rotation of polarization angle in respect to the structure. Additionally, the variation of Fermi level via electrostatic gating or chemical doping enables wide-range post-fabrication tunability of graphene-based structures, maintaining the same magnitude of the electromagnetic enhancement. The result of the numerical study clearly supports the concept of graphene-based SEIRA.

However, several challenges are imposed from the fabrication perspective. Proposed geometries are readily producible by commonly available tools, nevertheless, accessing the near-field coupling regime requires close positioning of plasmonic structures. The required 10 nm gap is at the limit of most of the conventional fabrication techniques. High-resolution methods are required to reliably reproduce such surfaces. Another fabrication-related issue arise from the two-dimensional periodicity of studied structures. A different approach to gating, compared to the one used for ribbon arrangement, is needed to effectively connect each plasmonic structure to a voltage source. The quality of fabricated material is also an issue. As it is demonstrated by the numerical data, the enhancement factor for the real synthesised graphene deviates from the ideal case significantly.

4.2. Experimental results

4.2.1. Pattering process optimization

Numerical study and optimization of graphene plasmonic antennae was followed by experimental fabrication and characterization of a graphene plasmonic device. An initial goal of the experimental work was to reproduce published experimental results achieved with a simple one-dimensionally-periodic nanoribbon geometry and then move towards the fabrication of more complex two-dimensional patterns.

At the first step, the capability of helium ion microscope for graphene nanopatterning was investigated in a series of exposure-dose experiments. In order to preliminary define the irradiation dose required for graphene milling, a number of collision trajectory simula-

tion were conducted for both available ions, i.e. He and Ne. After patterning, milled areas were characterized using atomic force microscopy. The results of collision trajectory simulations and focused ion beam patterning trials are demonstrated in the figure 4.7. Mode details on testing can be found in [93].
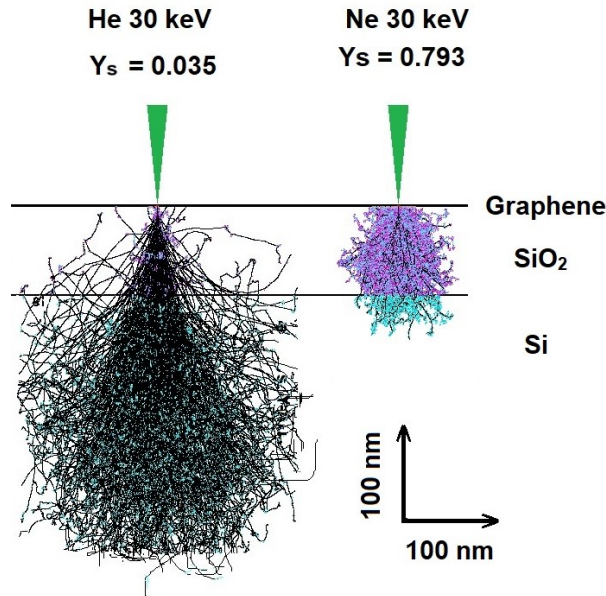

Figure 4.7: Computational simulation of collision trajectory distribution profile of helium (top) and neon (bottom) and associated sputtering yield Y_s.

The result of sputtering simulation shows that the yield values for both ions doubled compared to the published data for freestanding graphene [79]. This gain may be explained by considering the effect of substrate recoils. From the distribution of trajectories, it is also seen that helium ion, being a considerably smaller particle, penetrates further into the substrate causing less collision events (marked purple in the figure), ultimately producing an order of magnitude lower sputtering yield. Neon, on the other hand, produces a multitude of collision cascades occurring closer to the surface plane. That explains the higher sputtering yield and also indicates to a possible collateral damage to the surrounding environment.

AFM characterization revealed another drawback of using helium ion beam - parasitic surface deposition. As seen from the profile data, demonstrated in the figure 4.8, double cut-aways regions are not visible while an unexpected deposition of material is present, especially visible at large doses. One possible explanation for this phenomena is a deposition of carbon contamination as has been reported in [79]. Surprisingly, no parasitic growth was present in the case of Ne, and height profile demonstrates a well-defined ribbon area

between two milled regions. An increase in the exposure time produces a predictable variation of the depth of milled areas.
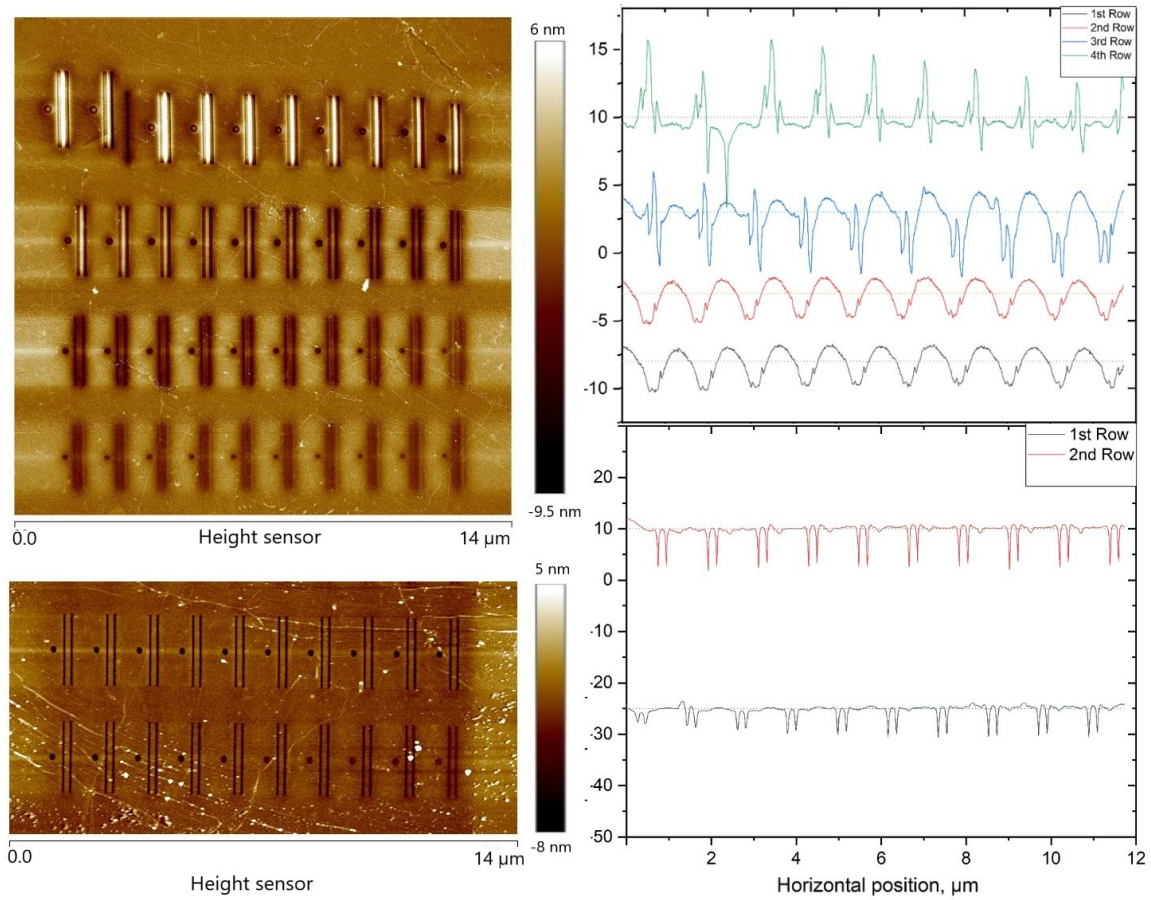

Figure 4.8: Atomic force mictroscope characterization of ion-milled graphene. Left side: Height map of graphene patterned with helium (top) and neon (bottom) beams. The dose increases from bottom to top and from right to left. For He beam - first row: 1 - 1.9 mC/cm^2 (step 0.1), second row: 2 - 11 mC/cm^2 (step 1), third row: 15 - 60 mC/cm^2 (step 5), forth row: 65 -110 mC/cm^2 (step 5)- For Ne beam - First row: 1 - 10 mC/cm^2 (step 1), second row: 11 -20 mC/cm^2 (step 1). Right side: Field profile measured for each row. Dashed line represents a "zero" level of corresponding profile curve

4.2.2. PLASMONIC DEVICE TESTING

At the next step a larger size nanoribbon pattern was fabricated on the actual chip using focused neon ion beam. Figure 4.9 demonstrates several microscopic images and the sur-

face profile of a nanoribbon-patterned area. According to AFM data, the pattern has been well-defined throughout the whole area. No substantial fabrication defects were found. The ribbons, defined between each pair of milled trenches, have consistent width, and the measured depth of exposed zones is 0.5 nm, which is sufficient to remove layer of graphene with 0.46 nm estimated thickness [21]. The averaged width of a single ribbon is 100 nm and the spacing between ribbons is 100 nm, with no significant deviation across the entire length of ribbons.
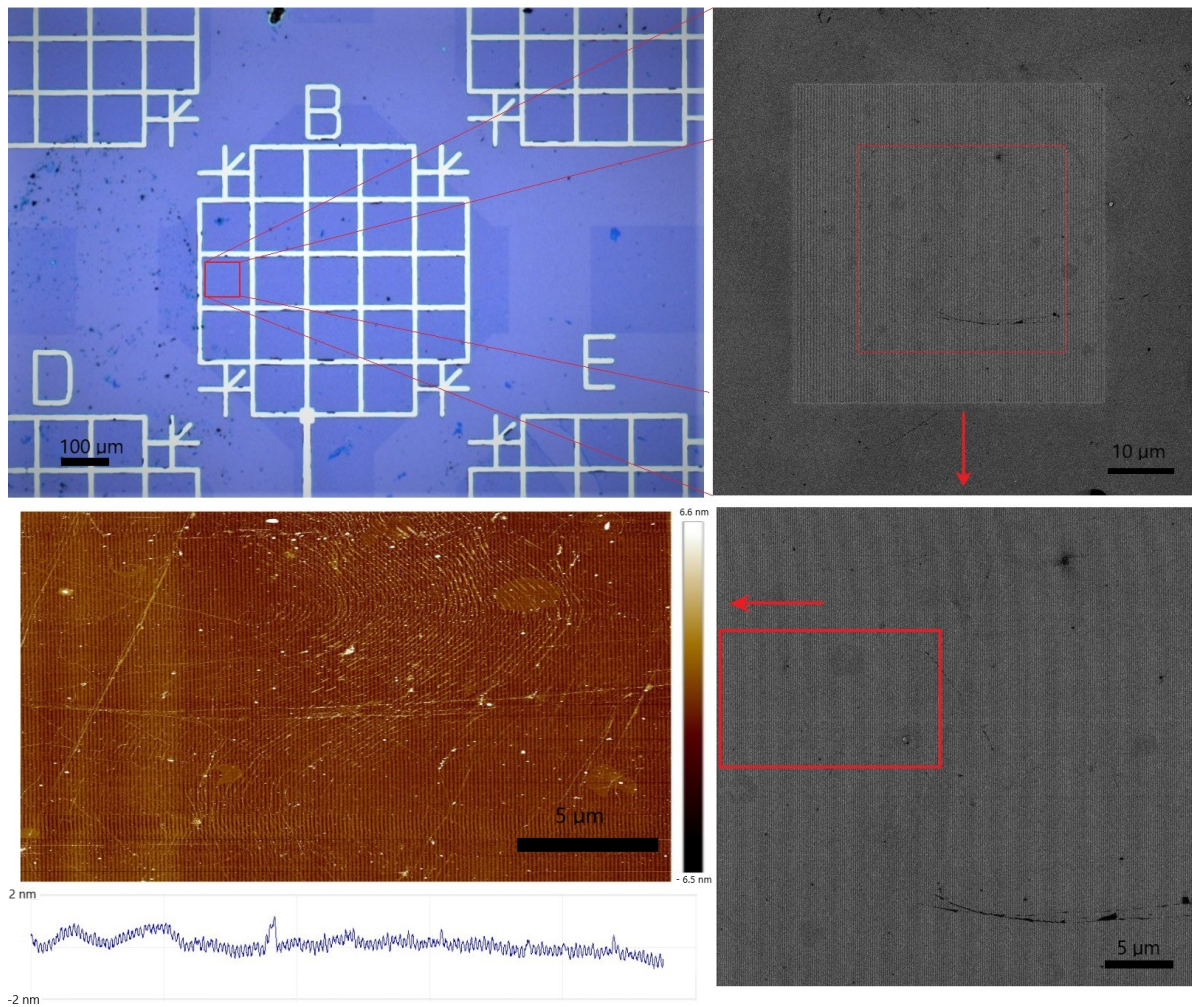

Figure 4.9: From the top-left image clockwise - optical microscope image of a single grid with graphene layer on top (darker areas); helium ion microscope image of the patterned area; A magnified HIM image of patterned area; AFM hight map and the averaged z-profile plot (below) of a randomly selected area

Finally, the chip was assembled into a carrier embedded into a PCB board equipped with

external circuit connections and the whole setup was characterized with FTIR microscopy. The result of FTIR absorbance measurements are presented in the figure 4.10. The variation observed at $\approx 1100\ \mathrm{cm}^{-1}$ seem to be continuously growing, in response to the increasing voltage, and reaching its peak value at 90 V. This result is controversial. On one hand the frequency, where deviation appears, well agrees with the published data on plasmonic response of graphene nanoribbons with the same width. [28]. On the other hand, the response to the voltage variation is different than expected. According to the published data, plasmonic peak should experience a spectral shift responding to the variation of the gate voltage. The measured peak, however, is static around a certain frequency and only growing in its magnitude. Hence, there is no certainty that the observed variation of the signal is caused by plasmons and further testing is required.
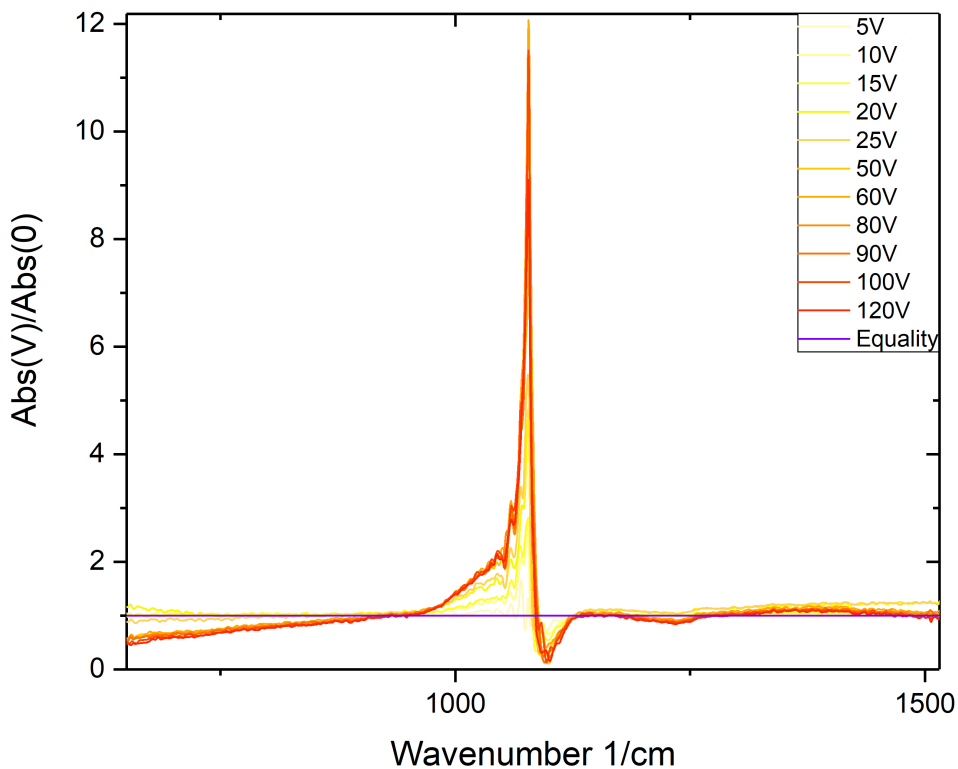

Figure 4.10: Infrared absorption signal of graphene nanoribbon (width - 100 nm) patterned area. Each spectrum correspond to the specified gate voltage divided by the absorption spectrum at 0V

At this point the experimental work was stopped due to external circumstances. Despite insufficiency of results, the attempt gave useful insights into the issues related to the fabrication procedure, the design of plasmonic device and measurement setup. From the fabrication perspective, HIM demonstrated stable patterning capability using Ne ions. A large aspect ratio ribbon patterns were successfully fabricated without any noticeable defects, and the overall milling process took less time to execute than conventional lithography. Also, since the process does not require resist, less contamination is introduced. However, the beam induced damage must be further investigated, as there is no published data regarding neon irradiation-related effects. Raman characterization and conductivity measurement of ion-patterned graphene as well as comparison with other fabrication methods may shed a light on that matter. Another question to address is the measurement setup. FTIR measurements were performed in the reflection mode, and it is known that graphene is mostly absorbing in the far-IR range. This explains a very low signal to noise ratio observed during the measurement procedure. Transmittance mode is preferable in the case of graphene. This will require a different design of chip carrier and thinner or different substrate, since transmittance of silicon abruptly drops at frequencies below 1000 cm^{-1}. As an additional method, a characterization with scanning near-field microscope can be utilized to study and visualize graphene plasmonic structures.

5. CONCLUSION

The aim of this work was to further investigate the potential of graphene as an active plasmonic material for the surface-enhanced infrared absorption spectroscopy. For the past two decades, graphene has been extensively studied from plasmonics perspective and it has demonstrated demonstrated broad spectral coverage, in the range from mid-IR to THz, and stronger field confinement compared to noble metals. As a semiconducting material, graphene also exhibits electrostatic tunability of plasmonic resonances. The combination of these features of graphene are highly desirable for spectroscopic applications. The concept of infrared spectroscopy utilizing graphene-based active plasmonic surface has already been proven by several research groups. Published results demonstrate sufficient performance for the analysis of solid and gaseous materials. All off these works use the simplest arrangement of plasmonic structures - the array of nanoribbons with periodicity along a single dimension. This choice is conditioned by a relatively simple fabrication process. However, as it is found in various publications concerning plasmonic materials and optimal geometries, spectroscopic applications mainly benefit from the local electromagnetic enhancement factor created in the tight spacing between plasmonic structures.

Therefore, the first goal of the work was to numerically study and optimize the selection of geometries from the perspective of produced enhancement factor and areal coverage. This part of the work was performed using FDTD computational method that was developed to solve electromagnetic field equation for various types of systems and geometries.

Numerical results demonstrated the capability of certain geometries, such as the bowtie, to produce the enhancement factor of the 10^5 order of magnitude. The enhanced field is confined within the 10 nm gap formed between extremities of each triangle. Two-dimensionality of plasmonic antennae enabled a resonance mode switching via changing the polarization angle of incident beam. Most of the proposed geometries were capable of supporting two different resonant modes, while the arrangement of rectangular tiles with two different width is able to produce three separate resonant peaks. Taking into account the tunability via Fermi level, the active surface can be adjusted to reach multiple frequency ranges during a single measurement procedure. Numerical simulation also revealed the drastic effect of the quality (quantified by electron scattering rate) of graphene on the local enhancement. While all conducted simulation assumed ideal graphene, the real-life values of scattering rate caused the local enhancement value to plunge by an order of magnitude.

The next stage of the work was to produce and characterize graphene-based active plasmonic surface. The fabrication procedure utilized novel approach for graphene patterning. Instead of standard lithographic techniques, that utilize photosensitive resist, direct

focused ion beam irradiation was used to selectively remove graphene via sputtering. Not only this method eliminates the necessity for coating graphene with the chemical layer that can introduce contamination, it also offers the superior resolution compared to widely-available "top-down" techniques. Exposure tests and AFM characterization demonstrated excellent performance of Ne ion beam that was able to accurately remove material from selected areas. Large area patterns were also correctly reproduced via this direct-write method. However, further testing of this method is required to evaluate collateral damage induced by high energy beam irradiation. Preliminary Monte Carlo simulation of sputtering process showed high probability of indirect damage, outside the focus spot, caused by recoiled ions and sputtered substrate material. Electrical and Raman characterization of graphene subjected to various ion irradiation doses may shed some light onto that matter.

The next step of the experimental work was to fabricate the sample device, containing patterned graphene and connected to an external circuit for electrostatic gating. For the first attempt, a ribbon pattern was chosen and the arrangement similar to the one reported in the literature was reproduced. The sample was tested with FTIR microscopy. Unfortunately, no convincing results can be reported. Observed spectra demonstrated a minor response to the voltage variation, however, the way the spectrum responded is dissimilar to the published data. One of the reason to distrust the results is an extremely low signal-to-noise ratio produced by the plasmonic setup. The issue with setup originates from inability to perform FTIR measurement in the transmission regime. It is known that, graphene is mostly absorbing incident electromagnetic light, hence the measurement of transmission rather than reflection are advisable. However, the final assembly of the sample did not allow transmission of light through it. Therefore, redesigning the sample assembly to enable transmission of infrared light would be the next step of the experimental work. Alternatively, near-filed scanning microscopy could be used to study plasmonic response of patterned structures.

On top of it all, the fabrication process should be further evaluated. The ion milling method may impair the quality of graphene causing an extreme damping of the signal. There is definitely a motivation for further investigation. Clearly, the concept of graphene-based SEIRA is a fully viable. Numerical studies of graphene plasmonic antennae showed that localized excitations are able to deliver substantial enhancement of confined field. However, main issues are related to the fabrication process. Being an atomically thin material, graphene is prone to defects and extremely sensitive to the surrounding environment. Therefore a further research on the quality of graphene patterning methods needs is required for the realization of a high enhancement graphene-based absorption spectroscopy.

REFERENCES

[1]   K. Paasch, "The history of optics: From ancient times to the middle ages", *DOPS-NYT*, vol. 1999, pp. 5–8, Jan. 1999.

[2]   A. Sommerfeld, "Ueber die fortpflanzung elektrodynamischer wellen lange eines drahtes", *Annalen der Physik*, vol. 303, pp. 233 –290, Mar. 2006.

[3]   R. Wood, "On a remarkable case of uneven distribution of light in a diffraction grating spectrum", *The London*, pp. 396–402, Sep. 1902.

[4]   U. Fano, "The theory of anomalous diffraction gratings and of quasi-stationary waves in metallic surfaces", vol. 31, pp. 213–222, Jul. 2020.

[5]   A. Hessel and A. Oliner, "A new theory of wood's anomalies on optical gratings", *Applied Optics*, vol. 4, pp. 1275–1297, Oct. 1965.

[6]   R. Ritchie, E. Arakawa, J. Cowan, and R. Hamm, "Surface-plasmon resonance effect in grating diffraction", *Physical Review Letters*, vol. 21, pp. 1530–1533, Nov. 1968.

[7]   E. Kretschmann and H. Raether, "Notizen: Radiative decay of non radiative surface plasmons excited by light", *Zeitschrift für Naturforschung A*, vol. 23, pp. 2135–2136, Dec. 1968.

[8]   A. Otto, "Excitation of nonradiative surface plasma waves in silver by method of frustrated total reflection", *European Physical Journal A*, vol. 216, pp. 398–410, Aug. 1968.

[9]   G. Mie, "Beiträge zur optik trüber medien, speziell kolloidaler metallösungen", *Ann. Phys.*, vol. 25, p. 377, Sep. 1908.

[10]   S. Pillai and M. Green, "Plasmonics for photovoltaic applications", *Solar Energy Materials and Solar Cells*, vol. 94, pp. 1481–1486, May 2010.

[11]   V. Sorger, D. Lanzillotti Kimura, R.-M. Ma, and X. Zhang, "Ultra-compact silicon nanophotonic modulator with broadband response", *Nanophotonics*, vol. 1, pp. 17–22, May 2012.

[12]   M. Hill, "Status and prospects for metallic and plasmonic nano-lasers", *JOSA B*, vol. 27, B36–B44, Nov. 2010.

[13]   S. Acimovic, M. Ortega, V. Sanz, J. Berthelot, J. Garcia-Cordero, J. Renger, S. Maerkl, M. Kreuzer, and R. Quidant, "LSPR chip for parallel, rapid, and sensitive detection of cancer markers in serum", *Nano letters*, vol. 14, 2636–2641, Apr. 2014.

[14]   X. Han, K. Liu, and C. Sun, "Plasmonics for biosensing", *Materials*, vol. 12, p. 1411, Apr. 2019.

[15] A. Haes, C. Haynes, A. McFarland, G. Schatz, R. Duyne, and S. Zou, "Plasmonic materials for surface-enhanced sensing and spectroscopy", *MRS Bulletin*, vol. 30, pp. 368–375, May 2005.

[16] M. Tame, K. R. Mcenery, S. Ozdemir, J Lee, S. Maier, and M Kim, "Quantum plasmonics", *Nature Physics*, vol. 9, pp. 329–340, Jun. 2013.

[17] G. Sartorello, A. Krasavin, A. Minovich, and A. Zayats, *Nonlinear Plasmonic Metasurfaces*. CRC Press, May 2020, pp. 117–146, ISBN: 9781351269766.

[18] S. Baieva, O. Hakamaa, G. Groenhof, T. Heikkilä, and J. Toppari, "Dynamics of strongly coupled modes between surface plasmon polaritons and photoactive molecules: The effect of the stokes shift", *ACS Photonics*, vol. 4, pp. 28 –37, Jan. 2017.

[19] P. Törmä and W. Barnes, "Strong coupling between surface plasmon polaritons and emitters: A review", *Reports on progress in physics. Physical Society (Great Britain)*, vol. 78, pp. 1–34, May 2014.

[20] K. MacDonald, Z. Sámson, M. Stockman, and N. Zheludev, "Ultrafast active plasmonics", *Nature Photonics*, vol. 3, pp. 55–58, Jan. 2009.

[21] K. Novoselov, A. Geim, S. Morozov, D. Jiang, Y. Zhang, S. Dubonos, I. Grigorieva, and A. Firsov, "Electric field effect in atomically thin carbon films", *Science (New York, N.Y.)*, vol. 306, pp. 666–669, Nov. 2004.

[22] L. Falkovsky, "Optical properties of graphene", *Journal of Physics: Conference Series*, vol. 129, p. 012 004, Oct. 2008.

[23] A. Castro Neto, F. Guinea, N. Peres, K. Novoselov, and A. Geim, "The electronic properties of graphene", *Review of Modern Physics*, vol. 81, 109–162, Oct. 2007.

[24] D. Papageorgiou, I. Kinloch, and R. Young, "Mechanical properties of graphene and graphene-based nanocomposites", *Progress in Materials Science*, vol. 90, pp. 75–127, Jul. 2017.

[25] L. Ju, B. Geng, J. Horng, C. Girit, M. Martin, Z. Hao, H. Bechtel, X. Liang, A. Zettl, Y Shen, and F. Wang, "Graphene plasmonics for tunable terahertz metamaterials", *Nature nanotechnology*, vol. 6, pp. 630–634, Sep. 2011.

[26] Y. Bludov, A. Ferreira, N. Peres, and M. Vasilevskiy, "A primer on surface plasmon-polaritons in graphene", *International Journal of Modern Physics B*, vol. 27, p. 1 341 001, Feb. 2013.

[27] J. Garcia de Abajo, "Graphene plasmonics: Challenges and opportunities", *ACS Photonics*, vol. 1, pp. 135–152, Feb. 2014.

[28] T. Low and P. Avouris, "Graphene plasmonics for terahertz to mid-infrared applications", *ACS nano*, vol. 8, pp. 1086–1101, Jan. 2014.

[29] F. Koppens, D. Chang, and J. Garcia de Abajo, "Graphene plasmonics: A platform for strong light-matter interactions", *Nano letters*, vol. 11, pp. 3370–3377, Aug. 2011.

[30] T. Stauber, "Plasmonics in dirac systems: From graphene to topological insulators", *Journal of physics. Condensed matter : an Institute of Physics journal*, vol. 26, p. 123 201, Mar. 2014.

[31] D. Rodrigo, O. Limaj, D. Janner, D. Etezadi, J. Garcia de Abajo, V. Pruneri, and H. Altug, "Mid-infrared plasmonic biosensing with graphene", *Science (New York, N.Y.)*, vol. 349, pp. 165–168, Jun. 2015.

[32] H. Hu, X. Yang, F. Zhai, D.-B. Hu, R. Liu, K. Liu, and Z. Sun, "Far-field nanoscale infrared spectroscopy of vibrational fingerprints of molecules with graphene plasmons", *Nature Communications*, vol. 7, p. 12 334, Jun. 2016.

[33] A. Marini, I. Silveiro, and J. Garcia de Abajo, "Molecular sensing with tunable graphene plasmons", *ACS Photonics*, vol. 2, pp. 876–882, Jul. 2015.

[34] H. Lai, F. Xu, Y. Zhang, and L. Wang, "Recent progress on graphene-based substrates for surface-enhanced raman scattering application", *Journal of Materials Chemistry B*, vol. 6, pp. 4008–4028, May 2018.

[35] Y. Li, H. Yan, D. Farmer, X. Meng, W. Zhu, R. Osgood, T. Heinz, and P. Avouris, "Graphene plasmon enhanced vibrational sensing of surface-adsorbed layers", *Nano letters*, vol. 14, 1573–1577, Feb. 2014.

[36] Y. Hu, A. López-Lorente, and B. Mizaikoff, "Graphene-based surface enhanced vibrational spectroscopy: Recent developments, challenges, and applications", *ACS Photonics*, vol. 6, 2182–2197, Jul. 2019.

[37] X. J. Lee, B. Y. Z. Hiew, k. c. Lai, L. Lee, S. Gan, S. Thangalazhy-Gopakumar, and S. Rigby, "Review on graphene and its derivatives: Synthesis methods and potential industrial implementation", *Journal of the Taiwan Institute of Chemical Engineers*, vol. 98, pp. 163–180, Nov. 2018.

[38] B. Sharma, R. Frontiera, A.-I. Henry, E. Ringe, and R. Duyne, "SERS: Materials, applications, and the future", *Materials Today*, vol. 15, pp. 16–25, Feb. 2012.

[39] B. Deng, Q. Guo, C. Li, H. Wang, X. Ling, D. Farmer, S.-J. Han, J. Kong, and F. Xia, "Coupling-enhanced broadband mid-infrared light absorption in graphene plasmonic nanostructures", *ACS Nano*, vol. 10, 11172–11178, Nov. 2016.

[40] H. Zhou, S. Su, W. Qiu, Z. Zhao, Z. Lin, p. qiu, and Q. Kan, "Multiple fano resonances with tunable electromagnetic properties in graphene plasmonic metamolecules", *Nanomaterials*, vol. 10, p. 236, Jan. 2020.

[41] S.-X. Xia, X. Zhai, L.-L. Wang, Q. Lin, and S.-C. Wen, "Localized plasmonic field enhancement in shaped graphene nanoribbons", *Optics Express*, vol. 24, pp. 16 336–16 348, Jul. 2016.

[42] J. Christensen, A. Manjavacas, S. Thongrattanasiri, F. Koppens, and J. Garcia de Abajo, "Graphene plasmon waveguiding and hybridization in individual and paired nanoribbons", *ACS nano*, vol. 6, pp. 431–440, Dec. 2011.

[43] S. Maier, *Plasmonics: Fundamentals and Applications*. Springer, New York, NY, Jan. 2007, pp. 1–223, ISBN: 978-0-387-33150-8.

[44] F. Rana, "Graphene terahertz plasmon oscillators", *Nanotechnology, IEEE Transactions on*, vol. 7, pp. 91 –99, Feb. 2008.

[45] K. Ki Young, *Plasmonics Principles and Applications*. IntechOpen, 2012, ISBN: 978-953-51-0797-2.

[46] P. Johnson and R. Christy, "Optical constants of noble metals", *Physical Review B*, vol. 6, pp. 4370 –4379, Dec. 1972.

[47] A. Bouhelier and G. Wiederrecht, "Excitation of broadband surface plasmon polaritons: Plasmonic continuum spectroscopy", *Phys. Rev. B*, vol. 71, p. 195 406, May 2005.

[48] A. Thilsted. (2013). Surface plasmon polariton sketch, [Online]. Available: `https://en.wikipedia.org/wiki/File:Sketch_of_surface_plasmon.png`. (accessed: 11.06.2020).

[49] K. Kolwas, A. Derkachova, and D. Jakubczyk, "Tailoring plasmon resonances in metal nanospheres for optical diagnostics of molecules and cells", in *Nanomedicine and Tissue Engineering: State of the Art and Recent Trends*. Jan. 2015, pp. 141 –183.

[50] J. Homola, *Surface Plasmon Resonance Based Sensors*. Springer, Berlin, Heidelberg, Jan. 2006, vol. 4, pp. 95–229, ISBN: 978-3-540-33918-2.

[51] J. Aizpurua and R. Hillenbrand, "Localized surface plasmons: Basics and applications in field-enhanced spectroscopy", *Plasmonics: From Basics to Advanced Topics*, vol. 167, pp. 151–176, Jun. 2012.

[52] S. Maier, P. Kik, H. Atwater, S. Meltzer, A. Requicha, and B. Koel, "Observation of coupled plasmon-polariton modes of plasmon waveguides for electromagnetic energy transport below the diffraction limit", *Proceedings of SPIE - The International Society for Optical Engineering*, vol. 4810, pp. 71 –81, Oct. 2002.

[53] B. Lamprecht, G. Schider, R. Lechner, H. Ditlbacher, J. Krenn, A. Leitner, and F. Aussenegg, "Metal nanoparticle gratings: Influence of dipolar particle interaction on the plasmon resonance", *Physical Review Letters*, vol. 84, pp. 4721–4724, Jun. 2000.

[54] N. Ly, K. Foley, and N. Tao, "Integrated label-free protein detection and separation in real time using confined surface plasmon resonance imaging", *Analytical chemistry*, vol. 79, pp. 2546–2551, Apr. 2007.

[55] A. Wark, H. j. Lee, and R. Corn, "Long-range surface plasmon resonance imaging for bioaffinity sensors", *Analytical chemistry*, vol. 77, pp. 3904–3907, Aug. 2005.

[56] Y. Li, H. j. Lee, and R. Corn, "Detection of protein biomarkers using RNA aptamer microarrays and enzymatically amplified surface plasmon resonance imaging", *Analytical chemistry*, vol. 79, pp. 1082–1088, Mar. 2007.

[57] S. Fang, H. j. Lee, A. Wark, and R. Corn, "Attomole microarray detection of microRNAs by nanoparticle-amplified SPR imaging measurements of surface polyadenylation reactions", *Journal of the American Chemical Society*, vol. 128, pp. 14 044–14 046, Dec. 2006.

[58] A. Yanik, M. Huang, O. Kamohara, A. Artar, T. Geisbert, J. Connor, and H. Altug, "An optofluidic nanoplasmonic biosensor for direct detection of live viruses from biological media", *Nano letters*, vol. 10, 4962–4969, Nov. 2010.

[59] T. Itoh, Y. Yamamoto, and Y. Ozaki, "Plasmon-enhanced spectroscopy of absorption and spontaneous emissions explained using cavity quantum optics", *Chem. Soc. Rev.*, vol. 46, pp. 3904–3921, Jun. 2017.

[60] J. Krenn, G. Schider, W. Rechberger, B. Lamprecht, A. Leitner, F. Aussenegg, and J.-C. Weeber, "Design of multipolar plasmon excitations in silver nanoparticles", *Applied Physics Letters*, vol. 77, pp. 3379–3381, Nov. 2000.

[61] P. Hanarp and D. Sutherland, "Optical properties of short range ordered arrays of nanometer gold disks prepared by colloidal lithography", *Journal of Physical Chemistry B*, vol. 107, 5768–5772, May 2003.

[62] L. Sherry, G. Schatz, R. Duyne, B. Wiley, and Y. Xia, "Localized surface plasmon resonance spectroscopy of single silver nanocubes", *Nano letters*, vol. 5, pp. 2034–2038, Nov. 2005.

[63] H. Wang, D. Brandl, F. Le, P. Nordlander, and N. Halas, "Nanorice: A hybrid plasmonic nanostructure", *Nano letters*, vol. 6, pp. 827–382, May 2006.

[64] C. Nehl, H. Liao, and J. Hafner, "Optical properties of star-shaped gold nanoparticles", *Nano letters*, vol. 6, pp. 683–688, May 2006.

[65] M. Knight and N. Halas, "Nanoshells to nanoeggs to nanocups: Optical properties of reduced symmetry core-shell nanoparticles beyond the quasistatic limit", *New Journal of Physics*, vol. 10, p. 105 006, Oct. 2008.

[66] J. Ziegler and R. Haglund, "Plasmonic response of nanoscale spirals", *Nano letters*, vol. 10, pp. 3013–3018, Aug. 2010.

[67] D. Rodrigo, A. Tittl, A. John-Herpin, O. Limaj, and H. Altug, "Self-similar multi-resonant nanoantenna arrays for sensing from near- to mid-infrared", *ACS Photonics*, vol. 5, 4903–4911, Oct. 2018.

[68] L. Brown, K. Zhao, N. King, H. Sobhani, P. Nordlander, and N. Halas, "Surface-enhanced infrared absorption using individual cross antennas tailored to chemical moieties", *Journal of the American Chemical Society*, vol. 135, pp. 3688–3695, Mar. 2013.

[69] P. A. Gonçalves and N. Peres, *An Introduction to Graphene Plasmonics*. World Scientific, Jun. 2016, pp. 1–464, ISBN: 978-981-4749-97-8.

[70] G. Hanson, "Dyadic green's functions and guided surface waves for a surface conductivity model of graphene", *Journal of Applied Physics*, vol. 103, pp. 064302 –064 302, Apr. 2008.

[71] M. Brown, M. Crosser, M. Leyden, Y. Qi, and E. Minot, "Measurement of high carrier mobility in graphene in an aqueous electrolyte environment", *Applied Physics Letters*, vol. 109, pp. 093 104–093 108, Aug. 2016.

[72] Y. Yao, Z. Li, Z. Lin, K.-s. Moon, J. Agar, and C. Wong, "Controlled growth of multilayer, few-layer, and single-layer graphene on metal substrates", *The Journal of Physical Chemistry C*, vol. 115, 5232–5238, Mar. 2011.

[73] L. Gomez, Y. Zhang, A. Kumar, and C. Zhou, "Synthesis, transfer, and devices of single- and few-layer graphene by chemical vapor deposition", *Nanotechnology, IEEE Transactions on*, vol. 8, pp. 135 –138, Apr. 2009.

[74] P. Somani and M. Umeno, "Planer nano-graphenes from camphor by CVD", *Chemical Physics Letters*, vol. 430, pp. 56–59, Oct. 2006.

[75] H. C. Lee, W. W. Liu, S.-P. Chai, A. Mohamed, A. Azizan, C.-S. Khe, N. H. Md Said, and U. Hashim, "Correction: Review of the synthesis, transfer, characterization and growth mechanisms of single and multilayer graphene", *RSC Adv.*, vol. 7, pp. 28 427–28 427, May 2017.

[76] O. Kapitanova, E. Kataev, D. Usachov, A. Sirotina, A. Belova, H. Sezen, M. Amati, M. Al-Hada, L. Gregoratti, A. Barinov, H. Cho, T. Kang, D. Vyalikh, D. Itkis, and L. Yashina, "Laterally selective oxidation of large-scale graphene with atomic oxygen", *The Journal of Physical Chemistry C*, pp. 27915 –27922, May 2018.

[77] M. Tripathi, A. King, G. Fratta, M. Meloni, M. Large, J. Salvage, N. Pugno, and A. Dalton, "Laser-based texturing of graphene to locally tune electrical potential and surface chemistry", *ACS Omega*, vol. 3, pp. 17 000–17 009, Dec. 2018.

[78] S. Kim, O. Dyck, A. Ievlev, I. Vlassiouk, S. Kalinin, A. Belianinov, S. Jesse, and O. Ovchinnikova, "Graphene milling dynamics during helium ion beam irradiation", *Carbon*, vol. 138, pp. 277–282, Jun. 2018.

[79] G. Hlawacek and A. Gölzhäuser, *Helium Ion Microscopy*. Springer, Jan. 2016, pp. 50–519, ISBN: 978-3-319-41988-6.

[80] B. Deng, Q. Guo, C. Li, H. Wang, X. Ling, D. Farmer, S.-J. Han, J. Kong, and F. Xia, "Coupling-enhanced broadband mid-infrared light absorption in graphene plasmonic nanostructures", *ACS Nano*, vol. 10, pp. 11172–11178, Nov. 2016.

[81] Z. Fei, M. Goldflam, J.-S. Wu, S. Dai, M. Wagner, A. McLeod, M. Liu, K. Post, S.-E. Zhu, G. Janssen, M. Fogler, and D. Basov, "Edge plasmons and plane plasmons in graphene nanoribbons", *Nano letters*, vol. 15, pp. 8271–8276, Nov. 2015.

[82] X. Yang, Z. Sun, T. Low, H. Hu, X. Guo, J. Garcia de Abajo, and P. Avouris, "Nanomaterial-based plasmon-enhanced infrared spectroscopy", *Advanced Materials*, vol. 30, p. 1 704 896, Mar. 2018.

[83] H. Wang, Z. Wang, J. Yang, C. Xu, Q. Zhang, and Z. Peng, "Ionic gels and their applications in stretchable electronics", *Macromolecular Rapid Communications*, vol. 39, p. 1 800 246, Jul. 2018.

[84] J. Chen, F. Yang, and R. Qiang, "FDTD method for periodic structures", in. Dec. 2017, pp. 6–1, ISBN: 9781315219370. DOI: 10.1201/9781420054262-6.

[85] W. yu and R. Mittra, "A conformal finite difference time domain technique for modeling curved dielectric surfaces", *Microwave and Wireless Components Letters, IEEE*, vol. 11, pp. 25 –27, Feb. 2001.

[86] E Palik, *Handbook of Optical Constant of Solids*. Elsevier, Jan. 1991, vol. 3, pp. 719–749, ISBN: 978-0-12-544422-4.

[87] G. Agrawal, *Nonlinear Fiber Optics*, 6th ed. Elsevier, Jan. 2012, pp. 124–125, ISBN: 9780123973078.

[88] V. Bliznyuk, D. Lajeunesse, and A. Boseman, "Application of helium ion microscopy to nanostructured polymer materials", *Nanotechnology Reviews*, vol. 3, pp. 130–140, Aug. 2014.

[89] J. Ziegler, M. Ziegler, and J. Biersack, "The stopping and range of ions in mater", *Nuclear Instruments and Methods in Physics Research Section B: Beam Interactions with Materials and Atoms*, vol. 268, pp. 1818–1823, Jun. 2010.

[90] W. Zhang, W.-C. Lu, M.-X. Song, K Ho, and C. Wang, "Tight-binding calculation studies of vacancy and adatom defects in graphene", *Journal of physics. Condensed matter : an Institute of Physics journal*, vol. 28, p. 115 001, Feb. 2016.

[91] Y. Kudriavtsev, A Villegas, A Godines, and R. Asomoza, "Calculation of the surface binding energy for ion sputtered particles", *Applied Surface Science*, vol. 239, pp. 273–278, Aug. 2004.

[92] A. Merrill, C. Cress, J. Rossi, N. Cox, and B. Landi, "Threshold displacement energies in graphene and single-walled carbon nanotubes", *Physical Review B - Condensed Matter and Materials Physics*, vol. 92, p. 075 404, Aug. 2015.

[93] A. Plyushch, "Graphene nanoribbon fabrication using focused ion beam lithography", University of Jyväskylä, Jan. 2020.

[94] S. Tasharrofi, S. Sadegh Hassani, and Z. Sobat, "Kelvin probe: Kelvin probe force microscopy as a tool for characterization of nanomaterials", in *CRC Concise Encyclopedia of Nanotechnology*. CRC Press, May 2015, pp. 391–397, ISBN: 978-1-4665-8034-3.

[95] E. Gazi, M. Baker, J. Dwyer, N. Lockyer, J. Shanks, R. Reeve, C. Hart, N. Clarke, and M. Brown, "A correlation of FTIR spectra derived from prostate cancer biopsies with gleason grade and tumour stage", *European urology*, vol. 50, pp. 750–760, Oct. 2006.

[96] S. Adhikari, D. Perello, C. Biswas, A. Ghosh, V. L. Nguyen, J.-H. Park, F. Yao, S. Rotkin, and Y. Lee, "Determining fermi level by absorption quenching of monolayer graphene by charge transfer doping", *Nanoscale*, vol. 8, pp. 18 710–18 717, Oct. 2016.

[97] J. Horng, C.-F. Chen, B. Geng, C. Girit, Y. Zhang, Z. Hao, H. Bechtel, M. Martin, A. Zettl, M. Crommie, Y Shen, and F. Wang, "Drude conductivity of dirac fermions in graphene", *Physical Review B*, vol. 83, p. 165 113, Jul. 2010.

A. NUMERICAL CONVERGENCE TESTING

The results of the error-optimization test for FDTD electromagnetic simulation of graphene. The absolute error (Δ_{sN})value is estimated by comparing the result of n-th simualtion with the first. Relative error (Δ_s) is computed by comparing n-th and n-1 simulations.
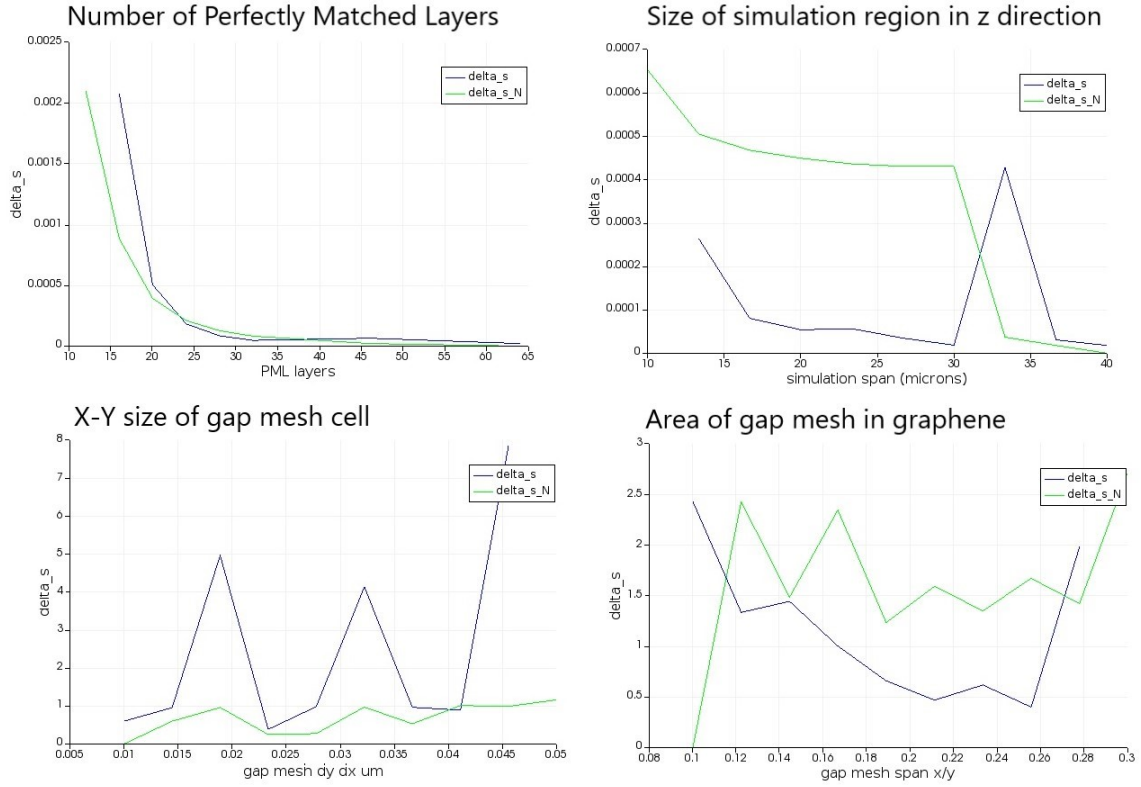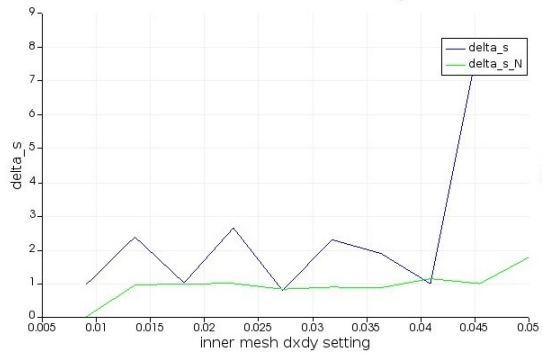
Span in z direction (um) of the fine mesh
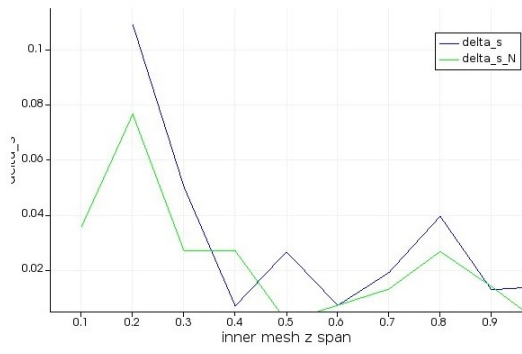
Size of cell of fine mesh in z direction
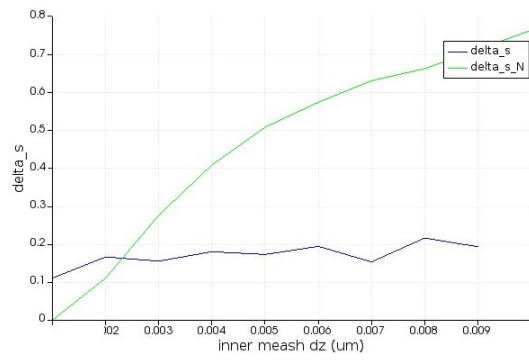
Cell size of the fine mesh in x-y direction

Outer mesh accuracy (x*5 points/wavelength)